

Probing the Extended Gaseous Regions of M31 with Quasar Absorption Lines^{*}

Sandhya M. Rao^{1†}, Gendith Sardane¹, David A. Turnshek¹, David Thilker², Rene Walterbos³, Daniel Vanden Berk^{4‡}, and Donald G. York⁵

¹*Department of Physics and Astronomy and PITTsburgh Particle physics, Astrophysics, and Cosmology Center (PITT PACC), University of Pittsburgh, Pittsburgh, PA 15260*

²*Center for Astrophysical Sciences, Johns Hopkins Univ., 3400 North Charles St., Baltimore, MD 21218*

³*Department of Astronomy, New Mexico State University, MSC 4500, Box 30001, Las Cruces, NM 88003*

⁴*Physics Department, St. Vincent College, Latrobe, PA 15650*

⁵*Department of Astronomy and Astrophysics, University of Chicago, Chicago, IL 60637*

ABSTRACT

We present *Hubble Space Telescope - Cosmic Origins Spectrograph* spectra of ten quasars located behind M31, selected to investigate the properties of gas associated with its extended disk and high velocity clouds (HVCs). The sightlines have impact parameters ranging between $b = 13$ kpc and 112 kpc. No absorption is detected in the four sightlines selected to sample any extended disk (or halo) gas that might be present in the outer regions of M31 beyond an impact parameter of $b > 57$ kpc. Of the six remaining sightlines, all of which lie at $b < 32$ kpc and within the $N_{HI} = 2 \times 10^{18}$ cm⁻² boundary of the H I disk of M31, we detect low-ionization absorption at M31 velocities along four of them (three of which include Mg II absorption). We also detect Mg II absorption from an HVC. This HVC sightline does not pass through the 21 cm disk of M31, but we detect additional Mg II absorption at velocities distinct from the HVC that presumably arises in the halo. We find that along sightlines where both are detected, the velocity location of the low-ion gas tracks the peak in 21 cm emission. High-ionization absorption is detected along the three inner sightlines, but not along the three outer sightlines, for which C IV data exist.

As inferred from high-resolution 21 cm emission line maps of M31's disk and extended regions, only one of the sightlines may be capable of harboring a damped Ly α system, i.e., with $N_{HI} \geq 2 \times 10^{20}$ cm⁻². This sightline has impact parameter $b = 17.5$ kpc, and we detect both low- and high-ion absorption lines associated with it. It is the strongest single Mg II $\lambda 2796$ absorption line that we detect, with rest equivalent width $W_0^{\lambda 2796} = 0.63$ Å.

The impact parameters of our observed sightlines through M31 are similar to the impact parameters of galaxies identified with Mg II absorbers at redshifts $0.1 < z < 1.0$ in a 2011 study by Rao *et al.* However, even if we only count cases where absorption due to M31 is detected, the Mg II $\lambda 2796$ rest equivalent width values are significantly smaller. In comparison, moderate-to-strong Mg II absorption from Milky Way gas is detected along all ten sightlines. Thus, this study indicates that M31 does not present itself as an absorbing galaxy which is *typical* of higher-redshift galaxies inferred to give rise to moderate-strength quasar absorption lines. M31 also appears not to possess an extensive large gaseous cross section, at least not along the direction of its major axis.

Key words: galaxies: individual: M31 - quasars: absorption lines

^{*} Based on observations made with the NOAO 2.1-m and the NASA/ESA *Hubble Space Telescope*.

[†] E-mail: srao@pitt.edu

[‡] Visiting Astronomer, Kitt Peak National Observatory, National

Optical Astronomy Observatory, which is operated by the Association of Universities for Research in Astronomy, Inc. (AURA),

1 INTRODUCTION

The standard paradigm for metal-line absorption systems in quasar spectra is that they arise in the extended gaseous halos/disks of galaxies well beyond their observable optical radii. However, with the exceptions afforded by gravitationally-lensed quasars, rarely is there more than one sightline passing in the vicinity of a galaxy. As such, the study of quasar absorption lines arising in extended gas associated with the great spiral galaxy in Andromeda (M31) represents a unique opportunity. M31's large extent on the sky means that many quasar sightlines should intercept its extended gas. For example, the $N_{HI} = 1.9 \times 10^{18}$ atoms cm^{-2} 21 cm emission contour around M31, as derived from the data discussed by Thilker et al. (2004), is approximately 5.0×1.5 square degrees on the sky (see Figure 1). We list some properties of M31 in Table 1. Quasar surveys have shown that there are as many as 18 quasars per square degree brighter than $g \sim 20$ at $z \lesssim 2.6$ (Richards et al. 2009, Abraham et al. 2012). Thus, there are likely to be on the order of 135 such quasars behind M31 within the boundaries of its observed 21 cm emission, and a factor of several more in its extended gaseous disk and halo regions. However, until now, quasar absorption lines have never been successfully used to study the extended gas of M31 because of the lack of sufficiently-bright, identified quasars.

Two of the most recognizable signatures of metal lines in quasar spectra are the Mg II $\lambda\lambda 2796, 2803$ and C IV $\lambda\lambda 1548, 1550$ doublets, which have been studied in numerous quasar absorption-line surveys. The first comprehensive study which demonstrated that galaxies at large impact parameters exist along the sightlines to low-redshift Mg II absorbers was by Bergeron and collaborators, e.g., Bergeron & Boissé (1991). They estimated that the average Mg II radius of a spherical gaseous envelope surrounding an L^* galaxy is $R^* \sim 3.5$ to $5.0 R_H$ (~ 55 to 80 kpc) at $z \sim 0.3$ for rest equivalent widths $W_0^{\lambda 2796} \geq 0.3 \text{ \AA}$, where R_H is the Holmberg radius. Others had made similar estimates (e.g., Lanzetta et al. 1987, Lanzetta & Bowen 1990, Steidel 1993). The recent survey of galaxies associated with Mg II absorbers at $0.1 < z < 1.0$ by Rao et al. (2011) showed that the gaseous extent of Mg II-selected absorbing galaxies could be as large as 100 kpc. At $z < 0.5$, Chen et al. (2010) find that the mean covering fraction for Mg II absorbers with $W_0^{\lambda 2796} \geq 0.3 \text{ \AA}$ within ~ 130 kpc of a $2L^*$ galaxy (for $h = 0.7$) is $\sim 70\%$. Therefore, if cross sections have remained constant since $z \sim 0.5$, then we might expect that gas giving rise to Mg II is likely to be present in the extended gaseous regions of M31 out to a radius of ~ 100 kpc or more, assuming it is a typical absorbing galaxy.

As described in §2, we obtained *Hubble Space Telescope (HST) - Cosmic Origins Spectrograph (COS)* spectra of ten quasars located behind M31 in order to investigate the properties of the gas in its extended disk and high velocity clouds (HVCs). We searched for Mg II, C IV, and other absorption lines to do this. In §3 we describe the results obtained from each spectrum. We discuss the results in §4 and end with a summary and conclusions in §5. This study indicates that M31 does not present itself as an absorbing galaxy which is

Table 1. M31 properties

Property	Value	Reference ^a
RA (2000)	00 ^h 42 ^m 44 ^s	1
Dec (2000)	+41°16'08''	1
Distance	752 ± 27 kpc	2
Inclination	78°	3
v_{sys}	-306 km/s	3
R_{opt}^b	22.3 kpc	4
m_B	4.16	4
L_B^c	$2.0L_B^*$	4,5
R_{21cm}^d	33 kpc	3
M_{virial}	$0.8 - 1.1 \times 10^{12} M_\odot$	6

^aReferences: 1. Evans et al. (2010); 2. Riess et al. (2012); 3. Corbelli et al. (2010); 4. de Vaucouleurs et al. (1991); 5. Cool et al. (2012); 6. Tamm et al. (2012)

^bOptical radius at B -band surface brightness $\mu_B = 25$ magnitudes per square arcsec.

^cAssuming $M_B^* = -19.92$ (Cool et al. 2012).

^dFrom the $N_{HI} = 1.9 \times 10^{18}$ atoms cm^{-2} contour (Figure 1).

typical of the higher-redshift galaxies inferred to give rise to moderate-strength quasar absorption lines.

2 OBSERVATIONS

2.1 Existing H I 21 cm Emission Observations

Since M31 is the nearest large spiral galaxy close to the Milky Way, it has been the subject of many observational studies. Specifically for this work, we will make reference to several results over the past decade from radio observational studies of M31's H I 21 cm emission. These are: the Green Bank Telescope (GBT) study of Thilker et al. (2004), which identified high-velocity clouds (HVCs) but at lower spatial resolution than later studies; the Westerbork Synthesis Radio Telescope (WSRT) study of Braun and Thilker (2004) which discovered the M31-M33 H I bridge, and of Westmeier et al. (2005), which focused on obtaining higher spatial resolution observations of HVCs; the WSRT study of Braun et al. (2009), which obtained observations over a wide field at high spatial resolution; and the study of Corbelli et al. (2010), which smoothed the data to lower spatial resolution in order to fit a tilted-ring model to M31's warped disk and study its rotation curve. At some level, all of this work was collaborative by various members of the same group, and in later studies they made use of results that could be derived from earlier data sets.

H I emission spectra were extracted from the Thilker et al. (2004) and Braun et al. (2009) datacubes along the sightlines toward our target quasars. These data, originally in units of Jy/beam, were converted to N_{HI} under the assumption of negligible H I opacity. This conventional assumption, while recently questioned by Braun et al. (2009) and Braun (2012) in the dense gaseous environment of the traditional optical disk and slightly beyond, is expected to be satisfied in the outer disk and halo environment. A more significant concern regarding the N_{HI} from observations of emission is the vastly different scale probed by the GBT and WSRT rel-

ative to COS. The maximum linear spatial resolution of the high resolution 21 cm observations is $\sim 50\text{--}100$ pc at the distance of M31. This scale is of order $\sim 10^5$ times larger than the linear spatial scale sampled in quasar ‘‘pencil-beam’’ absorption-line observations, where the pencil-beam has the scale of the UV continuum emitting region of the background quasar. Thus, N_{HI} values derived from 21 cm emission observations are averaged over a much larger spatial scale in comparison to those derived from quasar absorption-line spectra. Nevertheless, using 21 cm observations to derive average N_{HI} values along our sightlines, and noting the velocity range of detected emission, provides some important information.

As an aside, we note that it would be interesting if N_{HI} results derived from M31’s 21 cm emission data could someday be compared with N_{HI} determinations from Lyman series absorption seen in the UV spectra of background quasars. One could then get an H I column density measurement averaged over less than a milli-parsec region in M31, in comparison to the ~ 50 pc linear spatial scale offered by the radio observations. This would provide information on the homogeneity and size scale of H I absorbing regions in M31.

2.2 Optical Discovery Spectra of Quasars behind M31

We started this project by developing a list of quasars in especially desirable locations (see below) relative to M31. These were initially quasar candidates, since existing catalogs generally did not include quasars behind M31. The quasar candidates were selected from special plates of the SDSS, which were obtained specifically to find quasars behind the extended regions of M31 (Adelman-McCarthy et al. 2006). Of the 219 candidates, 108 were confirmed as quasars. Twenty-three of the 108 were spectroscopically confirmed during our October 2003 NOAO 2.1 m Gold Camera run at Kitt Peak. To make follow-up observations with HST-COS (§2.3 and §3) more feasible, we concentrated on finding brighter quasars. We also focused our search behind M31’s extended major axis to probe possible disk gas that could sample its outer rotation curve. See Figures 1 and 2, and Tables 1 and 2, for information on their locations relative to M31 and the discovery spectra. Quasars labeled 1 through 4 would sample any extended disk gas (or possibly halo gas) that is undetected in 21 cm emission; quasars 5, 6, 8, and 9 lie near the edge of detected 21 cm emission; the sightline towards quasar 7 passes through a high velocity cloud (HVC) in the circumgalactic environment of M31; and quasar 10 lies behind the 21 cm emission H I disk as well as two other HVCs. Importantly, owing to M31’s systemic velocity of -306 km s $^{-1}$ (Corbelli et al. 2010) and its direction of rotation, absorption originating on the southwest side of M31 will not be confused with Galactic absorption. Consequently, quasars 1 through 4 offer the best opportunities for observing extended disk gas and measuring M31’s rotation curve much farther out than possible with 21 cm emission observations. Unfortunately, while obtaining information on M31’s rotation curve at large galactocentric distance was one of the primary motivations for observing quasars 1 through 4, no M31 absorption near the expected velocity was detected in their UV spectra (§2.3 and §3). We note, however,

that higher quality observations might yet be able to detect gas at these locations. Observing quasars on the extended northeast side of M31 was avoided because of potential confusion with Galactic absorption.

2.3 HST-COS UV Spectroscopy

The HST-COS spectroscopic data were obtained during the period July-October 2010. Table 2 gives details of the quasars and the HST-COS observations. We decided to make a broad initial absorption-line survey in order to maximize the observed number of metal-line transitions we could reasonably cover within our allocation of 39 HST orbits.¹ The aim was to reach a signal-to-noise ratio which would enable us to detect Mg II and C IV absorption rest equivalent widths commonly seen in prior, large moderate-resolution quasar absorption-line surveys. Therefore, we did not use higher-resolution COS gratings. However, it would indeed be worthwhile to perform follow-up spectroscopy of a number of our detections at higher spectral resolution and signal-to-noise ratios.

The COS gratings used in this study along each sightline are specified in Table 2. The near ultraviolet (NUV) G230L grating has a resolution of 2 pixels or ~ 0.82 Å at the wavelength of the Mg II $\lambda\lambda 2796,2803$ doublet, which corresponds to ~ 87 km s $^{-1}$ on a velocity scale. The far ultraviolet (FUV) G140L grating has a resolution of 7 pixels or ~ 0.55 Å at the wavelength of the C IV $\lambda\lambda 1548,1550$ doublet, which corresponds to ~ 106 km s $^{-1}$. Given the redshifts of the quasars, we should note that in certain wavelength regions there is the possibility of contamination by Ly α forest absorption. For example, Ly α forest absorption would potentially be visible near any Galactic or M31 Mg II absorption when the quasar’s redshift is higher than $z_{em} \sim 1.3$ (e.g., in quasar number 4) and near any Galactic or M31 C IV absorption when the quasar’s redshift is higher than $z_{em} \sim 0.27$ (e.g., in all quasars except number 9). However, according to Weymann et al. (1998), the incidence of Ly α forest absorption lines with rest equivalent widths ≥ 0.24 Å at these relatively low redshifts is typically only about one line per 30 Å (about one line per 3200 km s $^{-1}$), so we did not necessarily anticipate too much confusion due to overlapping Ly α forest absorption. There might also be overlapping absorption due to unidentified metal-line systems. In §3 we note instances where Ly α forest absorption or other overlapping unidentified absorption appears to be a confusing factor.

Seven quasars were observed with both the NUV and FUV gratings, while three were targeted with the NUV grating alone. These three had low FUV fluxes based on the *GALaxy Evolution eXplorer* (GALEX) telescope measurements, and so they were not observed. The NUV grating covers Fe II, Mn II, Mg II and Mg I transitions, while the FUV grating covers C IV, Si IV and several lower-ion transitions, as described in §3.

Pipeline flux-calibrated and wavelength-calibrated spectra were used for all the measurements, and no additional calibrations or re-calibrations were carried out.

¹ Parallel imaging data were also obtained. These will be discussed in Thilker et al. (in prep.).

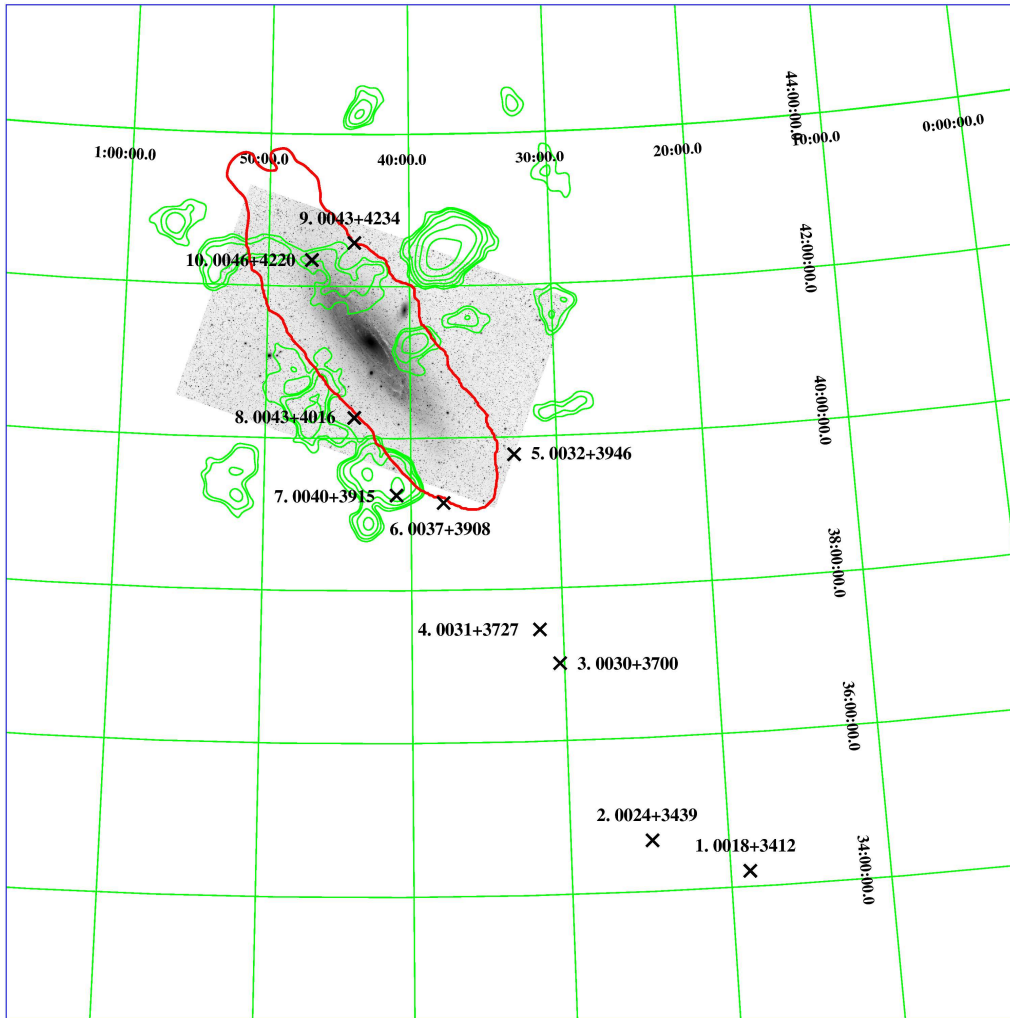


Figure 1. Location of the ten quasars that were observed with *HST-COS*. An optical image of M31 is shown in the background along with 21 cm emission maps showing the disk gas and HVCs. The red contour is 21 cm emission at 1 Jy km/s, or an HI column density of $N_{HI} = 1.9 \times 10^{18} \text{ cm}^{-2}$. Higher column density contours interior to this are not shown. High velocity cloud contours from Thilker et al. (2004) are shown in green. The scale at the distance of M31 is $13.2 \text{ kpc deg}^{-1}$. The innermost (8. 0043+4016) and outermost (1. 0018+3412) quasars are at projected distances (impact parameters) of $b = 13.4 \text{ kpc}$ and $b = 111.9 \text{ kpc}$ from M31's center. See Tables 1 and 2.

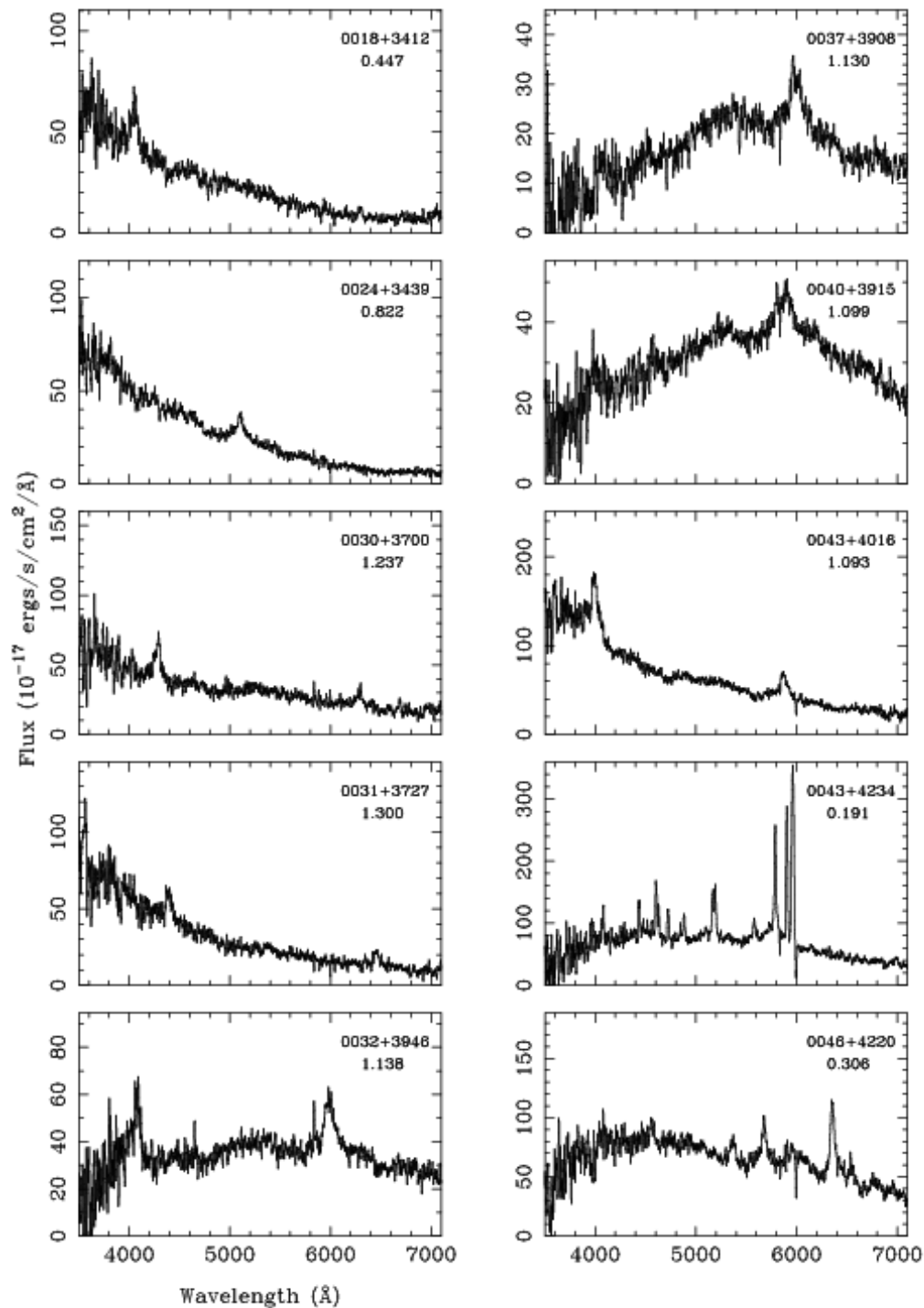


Figure 2. KPNO 2.1m Gold Camera discovery spectra of the ten quasars that were observed with HST-COS. The quasar name and emission redshift are noted in each panel.

Table 2. Quasars observed with HST-COS

Quasar	RA (2000) h m s	Dec (2000) ° ' "	Map ID ^a	z_{em}	SDSS <i>u</i> mag	b (kpc) ^b	COS G140L Exp time (s)	COS G230L Exp time (s)	Sightline notes ^c
0018+3412	00 18 47.45	+34 12 09.6	1	0.447	17.7	111.9	3446	5646	extended disk
0024+3439	00 24 50.05	+34 39 42.8	2	0.822	18.1	98.6	...	5092	extended disk
0030+3700	00 30 17.43	+37 00 54.3	3	1.237	17.5	64.4	4054	3191	extended disk
0031+3727	00 31 32.37	+37 27 51.8	4	1.300	18.5	57.6	4455	2246	extended disk
0032+3946	00 32 55.70	+39 46 19.3	5	1.138	18.6	31.5	...	10324	edge of 21 cm disk
0037+3908	00 37 48.00	+39 08 58.7	6	1.130	18.4	30.5	...	10354	edge of 21 cm disk
0040+3915	00 40 59.03	+39 15 12.3	7	1.099	18.5	26.9	6293	11101	HVC + 21 cm disk edge
0043+4016	00 43 52.45	+40 16 29.4	8	1.093	18.2	13.4	7073	5537	edge of 21 cm disk
0043+4234	00 43 54.98	+42 34 30.4	9	0.191	18.0	17.4	3555	6137	edge of 21 cm disk
0046+4220	00 46 55.52	+42 20 50.1	10	0.306	18.1	17.5	2572	5217	2 HVCs + 21 cm disk

^aQuasar IDs in order of increasing RA.^bProjected distance from galactic center assuming that the center of M31 is at (00^h42^m44^s, +41°16′08″) and that the distance to M31 is 752 kpc. See Table 1.^cSee Figure 1.

The wavelength scale is heliocentric, and measured velocity offsets relative to a transition of interest are made on this scale. Before making absorption-line measurements, the FUV spectra were re-binned to two pixels per resolution element and all spectra were normalized using an interactive algorithm which fitted splines to a quasar’s observed continuum plus broad emission lines to derive a pseudo-continuum. We used the pipeline-provided standard deviation in flux to calculate the 1σ error in the normalized flux. When reporting errors in equivalent width measurements, we do not include (propagate) any errors that might arise during the process of defining a pseudo-continuum.

3 RESULTS

Figures 3 – 12 show the pseudo-continuum-normalized spectra near the predicted locations of metal lines along the ten sightlines, and Table 3 gives the measured metal-line absorption rest equivalent widths or upper limits for both M31 and Galactic lines. To make these measurements, heliocentric velocity locations for the absorbing gas had to be determined. The procedure for this is discussed below and the results on velocity offsets are given in Table 4.

For the low-ion transitions, the narrow Mn II lines (when present) allow for a more accurate determination of the velocity centroid of Galactic gas since they are well-fitted by single Gaussians. Therefore, the velocity offsets of low-ion Galactic absorption lines are defined by the centroids of Galactic Mn II $\lambda 2576$ absorption for sightlines 2, 8, 9, and 10. The centroids of Galactic Mg II $\lambda 2796$ are used to define the velocity offsets of absorption along other sightlines. The wavelength interval covered by the *COS-FUV* spectra includes transitions due to Si II, O I, C II, C II*, Fe II, and Al II. The centroids of these low-ion lines were fixed at the velocities determined from either the Mn II $\lambda 2576$ line or Mg II $\lambda 2796$ as indicated above. The velocity offset results were used to deblend the Mg II and Fe II lines along sightlines 9 and 10 into M31 and Galactic contributions. This was necessary because these two sightlines lie in the northeast

(receding half) of M31’s rotating disk. As a result, the velocity offset differences of M31 and Galactic gas along these sightlines is only $\sim 150 \text{ km s}^{-1}$. Since velocity offset differences are much larger for the other sightlines, there was little confusion when separating those contributions. In the panels for each figure, dash-dot vertical lines are drawn at the determined velocity offsets of M31 and Galactic gas.

The only high-ion transitions detected in our spectra are due to C³⁺ and Si³⁺. The velocity centroids of Gaussians fitted to the C IV $\lambda 1548$ lines were allowed to vary since low-ion and high-ion absorption lines are not *a priori* required to have the same velocity centroids or line widths. The C IV $\lambda 1550$ line and Si IV lines were then constrained to have the same velocity locations and widths as the C IV $\lambda 1548$ line, within the uncertainties and resolution of the data. Inspection of the final fits suggests that this was a reasonable constraint.

The 1σ error in the normalized flux is shown in the figures as a black dotted line. M31 and Galactic absorption transitions that are identified at a level of significance $> 2\sigma$ are indicated in the figures by red profiles. A $> 2\sigma$ rest equivalent width detection threshold is an appropriate criterion for identifying absorption because we already know the approximate velocity location of M31 absorption (e.g., from M31’s 21 cm emission). We also searched for significant absorption in a wider velocity window. Gaussian profiles are fitted to detected absorption. If more than one Gaussian is required to fit the data, we show the individual Gaussians as red dashed profiles, visible above the solid red profile. In the absence of multiple Gaussians, the red solid profile will lie on top of the red dashed profile, and the red dashed profile will not be visible. However, the measurements indicated by the red dashed profiles are what we report in Tables 3 and 4. As noted earlier, the positions of most low-ion lines are fixed by the centroid of either the Mn II $\lambda 2576$ or the Mg II $\lambda 2796$ line; however, their widths are allowed to vary in order to obtain the best fit. In a few cases, even the velocity offsets had to be allowed to vary up to one resolution element in order to obtain a satisfactory fit. Also, while per-

forming the fits, we identified some absorption in the spectra which were likely blends resulting from a real M31 or Galactic absorption line plus overlapping or nearby absorption due to, for example, Ly α forest absorption, some other unrelated absorption, or even related absorption such as C II λ 1334.5 and C II* λ 1335.7. When this happened, we fitted Gaussians to these nearby absorption components in order to better isolate the M31 and Galactic absorption transition of interest. We refer to this as deblending. However, when we report results in Tables 3 and 4, as noted earlier, only absorption taken to be due to the designated transition of interest in M31 or the Galaxy is reported and shown on the figures. Other nearby absorption lines which were fitted in order to isolate M31 and Galactic gas are shown as green dashed Gaussian profiles. The identifications and measurements of M31 and Galactic lines in the presence of confusing overlapping or nearby absorption should be considered less secure.

When a line is not detected (i.e., the detection is $< 2\sigma$) at its expected velocity offset, or nearby absorption not due to the transition of interest appears to be present, a red dotted Gaussian profile with FWHM equal to the spectrograph resolution (i.e., $\sim 0.82 \text{ \AA}$ or $\sim 87 \text{ km s}^{-1}$ for the NUV lines and $\sim 0.55 \text{ \AA}$ or $\sim 106 \text{ km s}^{-1}$ for the FUV lines) is shown on the figures to indicate the reported upper limit. If no overlapping or nearby confusing absorption is present, this is just the 2σ upper limit on equivalent width generated from the error in normalized flux. However, if overlapping or nearby absorption is present, the upper limit is determined from the strength of this overlapping or nearby absorption. Lacking evidence that a low-oscillator-strength transition should be present along a particular sightline, we would attribute any significant detected absorption as due to overlapping absorption, and list it as an upper limit.

In cases where the velocity of an M31 absorption line overlaps with the velocity of a different Galactic absorption line, for example, the M31 C IV λ 1550 and the Galactic C IV λ 1548 lines, or the M31 Si II λ 1304 and the Galactic O I λ 1302 lines along sightline numbers 1, 3, and 4 (Figures 3, 5, and 6), we assign the absorption to the Galactic absorption system. The measurement is listed in Table 3 only for the Galactic absorption line.

The bottom panels for sightlines 5 through 10 (Figures 7 – 12) show H I 21 cm emission profiles extracted from the GBT data of Thilker et al. (2004). The intensities are scaled to accentuate the very weak emission signal from M31. The dash-dot horizontal line drawn in each 21 cm panel marks the location of zero intensity. The H I 21 cm emission disk of M31 extends out to $\sim 33 \text{ kpc}$ as determined from the $N_{HI} = 1.9 \times 10^{18} \text{ cm}^{-2}$ column density contour (Figure 1), and no H I 21 cm measurements exist at the positions of quasars 1 through 4. Therefore, to estimate equivalent width upper limits for these four sightlines, we have assumed that M31's 21 cm rotation curve is flat at large galactocentric distances and we extrapolate the sightline 21 cm emission velocity out to the positions of quasars 1 through 4 to predict a probable velocity location of absorbing gas. Note that M31 is nearly edge-on and inclined $\sim 78 \text{ deg}$ on the plane of the sky. Thus a very small inclination correction is needed since $\sin(78) = 0.978$. Then the assumption of a flat rotation curve suggests that if metal-line absorption is present in M31's outer regions, we might find it near a heliocentric

velocity location of $\sim -525 \text{ km s}^{-1}$. This is where we determine M31 equivalent width upper limits for sightlines 1 through 4. We note that the choice of where to measure potential absorption in the four outer sightlines is purely an algorithmic decision given that flat rotation curves exist. We also considered the Tamm et al. (2012) study which derives a rotation curve out to a galactocentric radius of $\sim 500 \text{ kpc}$. They employ, among other diagnostics, observations of stellar streams (Fardal et al. 2006) and satellite galaxies (Tollerud et al. 2012) which yield rotational velocities of $\sim 160 \text{ km s}^{-1}$ near the position of our outermost sightline. This translates to a heliocentric velocity of -466 km s^{-1} since our outer sightlines lie on the approaching, SW, side of M31. This is well within one resolution element ($\S 2.3$) of our assumed velocity location of -525 km s^{-1} . Therefore, we are confident that we have not missed any absorption from gas in M31 along the outer four sightlines that is above our detection limits.

Tables 3 and 4 summarize all of the measurements and upper limits, both for M31 and the Milky Way Galaxy. A discussion of individual sightlines follows (see Figures 3 – 12), with emphasis on what they reveal about M31 gas. The discussions are presented in order of increasing sightline right ascensions. This ordering generally follows decreasing impact parameter, b , except for the last three sightlines which all have $13 < b < 18 \text{ kpc}$. At the beginning of each discussion we indicate the maximum wavelength at which Ly α forest absorption might cause blending and confusion, $\lambda_{forest} \sim 1216(1 + z_{em}) \text{ \AA}$.

1. 0018+3412 ($b = 111.9 \text{ kpc}$, $\lambda_{forest} < 1760 \text{ \AA}$, Fig. 3):

No significant M31 absorption is detected along this sightline, and H I 21 cm emission maps of M31 do not extend this far out. Therefore, rest equivalent width upper limits on absorption were measured at -525 km s^{-1} as described earlier. At this velocity location, the red dotted Gaussian lines show the velocity positions and rest equivalent widths of hypothetical unresolved absorption lines with 2σ levels of significance, and these are the upper limits reported in Table 3. Galactic absorption is clearly present. Suspected confusion (blending) due to overlapping Ly α forest absorption is apparent for the Si II λ 1260, Si II λ 1304, O I λ 1302, C II λ 1334, and C IV λ 1550 Galactic absorption lines. The method we used to measure such cases was discussed above.

2. 0024+3439 ($b = 98.6 \text{ kpc}$, $\lambda_{forest} < 2216 \text{ \AA}$, Fig. 4):

As in the previous sightline, no significant M31 absorption is detected, and H I 21 cm emission maps do not extend this far out, so upper limits were measured at a velocity location of -525 km s^{-1} . Only NUV spectra of this quasar were obtained. Therefore, for example, the C IV region was not observed. A Galactic Mn II λ 2576 line is detected at a level of significance of $\sim 3\sigma$, however the two weaker members of the triplet are not detected at $> 2\sigma$. Galactic Mg II and Fe II absorption are clearly detected.

3. 0030+3700 ($b = 64.4 \text{ kpc}$, $\lambda_{forest} < 2720 \text{ \AA}$, Fig. 5):

Again, no significant absorption lines from M31 are detected at or near -525 km s^{-1} , and the 21 cm emission maps do not extend out this far. Among the significant Galactic absorption lines that are detected, the measurements of Si II λ 1260, Si IV λ 1393, C IV λ 1548 and Fe II λ 2586 were made in the presence of overlapping unrelated absorption using the method described earlier. While only the stronger members

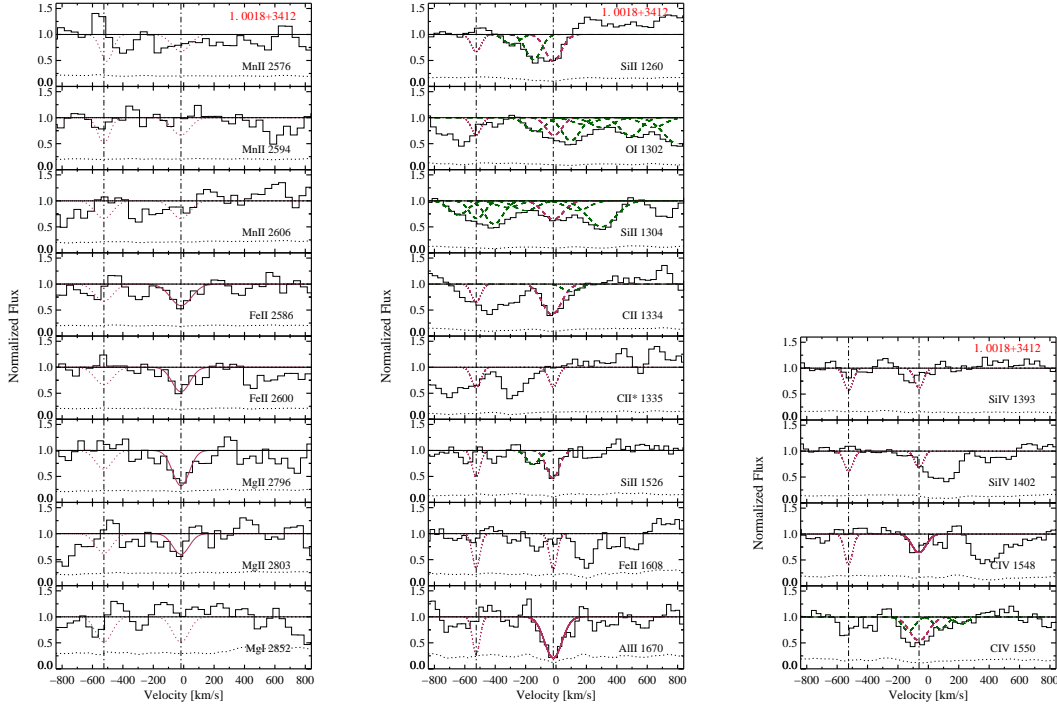


Figure 3. Normalized spectra versus velocity for the labeled transitions in the spectra of 0018+3412. The black dotted line is the 1σ error spectrum. All velocities are heliocentric. The vertical dot-dashed lines are Milky Way (near 0 km/s) and M31 detected or assumed velocities. See Table 3. Fits to M31 and Galactic absorption lines detected at a significance $> 2\sigma$ are shown as heavy dashed (if part of a blend) or solid red lines. See text. Dotted red lines indicate 2σ upper limits. Green dashed lines are components within a blend that are unrelated to M31 or Galactic absorption.

of the Galactic Si IV and C IV doublets are detected, the rest equivalent width upper limits of the weaker members of these doublets are consistent with their expected strengths based on $f\lambda$ values. In addition to the detected Galactic metal absorption lines, at least two partial Lyman limit absorption systems are present in the spectrum. One at $z \sim 0.5$ is clearly visible in the FUV observation (not shown). Based on the difference in flux level between the FUV and NUV observations, and the presence of some strong Ly α forest absorption near and just shortward of the Ly α broad emission line, at least one other Lyman limit absorption system is likely to be present at $1.21 < z < 1.24$. However, it is not directly visible in our observations because it falls in the wavelength gap between the FUV and NUV spectra.

4. 0031+3727 ($b = 57.6$ kpc, $\lambda_{forest} < 2797$ Å, **Fig. 6**):

As with the first three sightlines, no significant absorption lines from M31 gas are seen, and the 21 cm emission map does not extend out this far. M31 upper limits were estimated at -525 km s $^{-1}$ for both the high and low ions. Galactic absorption is clearly detected for some transitions, but the measurements of Si II $\lambda 1260$, C II $\lambda 1334$, Si II $\lambda 1526$, Fe II $\lambda 1608$, and Fe II $\lambda 2600$ required deblending due to the presence of unrelated overlapping absorption.

5. 0032+3946 ($b = 31.5$ kpc, $\lambda_{forest} < 2600$ Å, **Fig. 7**):

Only NUV spectra were obtained for this quasar. An M31 Mg II $\lambda 2796$ absorption line with a significance of 2σ at

a heliocentric velocity of -453 km s $^{-1}$ appears to be present (see Table 3), however a corresponding 2-pixel-wide absorption feature near the expected position of Mg II $\lambda 2803$ has a significance $< 2\sigma$. If present, this absorption may originate at the southwest edge of M31's disk (see Figure 1). Apart from strong Galactic emission, the GBT 21 cm data along this sightline (bottom panel of Figure 7) shows evidence for M31 emission between -509 and -459 km s $^{-1}$. Although the resolution of the NUV spectrum is ~ 0.82 Å (~ 87 km s $^{-1}$) at the position of Mg II, the centroid of the absorption line can be estimated with an uncertainty of ~ 6 km s $^{-1}$ (see §4). Thus, the identified Mg II $\lambda 2796$ feature at -453 km s $^{-1}$ is near the maximum velocity of observed 21 cm emission. Keeping in mind the limitations of using H I 21 cm emission observations to determine H I column densities (§2.1), we find $N_{HI} \approx 2.5 \times 10^{18}$ atoms cm $^{-2}$ along this sightline. Very significant Galactic Mg II and Fe II absorption is detected along this sightline, but the Galactic Fe II $\lambda 2586$ line was deblended to separate it from unrelated nearby absorption.

6. 0037+3908 ($b = 30.5$ kpc, $\lambda_{forest} < 2590$ Å, **Fig. 8**):

Only NUV spectra were obtained for this quasar. Absorption from M31 gas is not detected. However, apart from the strong Galactic emission, the GBT data along this sightline reveal M31 21 cm emission between -542 and -475 km s $^{-1}$ (bottom panel of Figure 8), with an integrated column density of $N_{HI} = 2.5 \times 10^{18}$ atoms cm $^{-2}$ (see §2.1). The

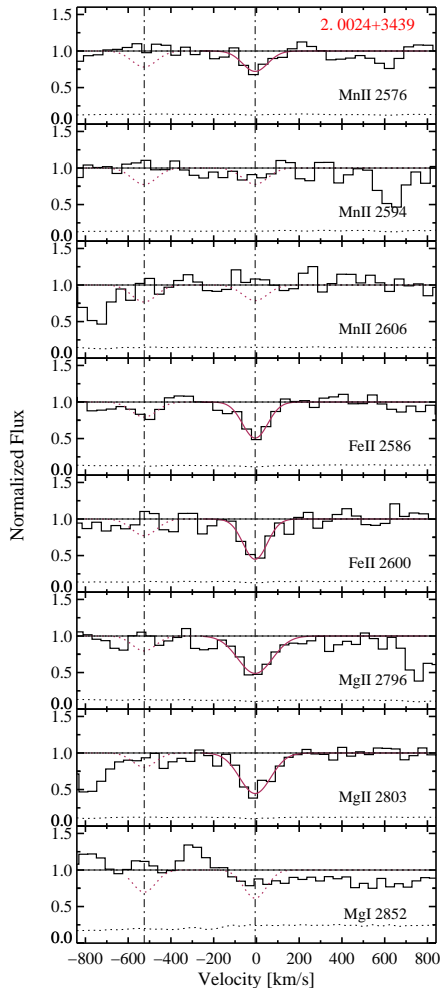


Figure 4. Same as Figure 3, but for 0024+3439. No FUV spectra of this quasar were obtained.

2σ upper limits on M31 absorption are made at the central velocities predicted by the observed M31 21 cm emission. Very significant Galactic Mg II and Fe II absorption is detected along this sightline. The Galactic Fe II $\lambda 2586$ and Fe II $\lambda 2600$ lines were deblended to separate them out from unrelated nearby absorption.

7. 0040+3915 ($b = 26.9$ kpc, $\lambda_{forest} < 2552$ Å, **Fig. 9**):

Only the velocity profiles in the vicinity of Mg II and Mg I are visible in our observations for two reasons. First, the quasar spectrum exhibits intrinsic broad absorption lines (BALs) and the N V BAL trough overlaps the Mn II and Fe II absorption-line regions. This prevents useful measurements of M31 and Galactic lines in those regions. Second, the FUV spectrum shows no useful continuum flux, possibly due to strong shorter-wavelength BALs and/or overlapping intervening Lyman limit absorption. Mg II $\lambda 2796$ due to M31 gas appears as two absorption components in the NUV spectrum. The noise characteristics of the spectrum are worse in the corresponding Mg II $\lambda 2803$ region, and two absorption components are not seen (a single Gaussian was

fitted to the absorption), but we give this lower weight due to the higher noise. The two vertical dash-dot lines at -389 km s $^{-1}$ and -513 km s $^{-1}$ mark the velocity positions of the two M31 Mg II $\lambda 2796$ absorption components. The sightline passes through an HVC (see Figure 1), whose 21 cm emission profile can clearly be seen in the bottom panel of the figure peaking at ~ -500 km s $^{-1}$. The GBT data reveal that this 21 cm emission extends between -542 and -442 km s $^{-1}$. Thus, the two Mg II absorption components at -389 km s $^{-1}$ and -513 km s $^{-1}$ may correspond to M31 halo gas and HVC gas, respectively, with the halo component showing no apparent 21 cm emission. From the WSRT 21 cm emission data, the integrated H I column density in the HVC is estimated to be $N_{HI} = 9.5 \times 10^{19}$ atoms cm $^{-2}$ (see §2.1). Very significant Galactic Mg II absorption is present along this sightline.

8. 0043+4016 ($b = 13.4$ kpc, $\lambda_{forest} < 2545$ Å, **Fig. 10**):

This is the lowest impact parameter sightline. M31 low-ion absorption from Si II $\lambda 1260$ and C II $\lambda 1334$ is detected, and high-ion absorption from C IV $\lambda 1548$ is detected, but

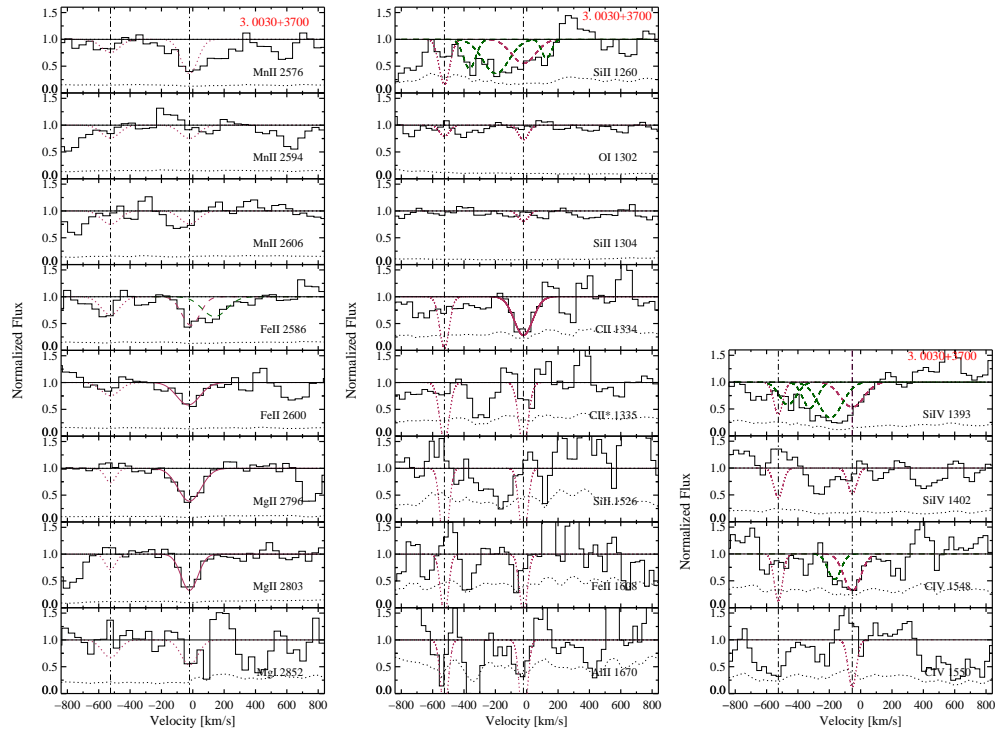


Figure 5. Same as Figure 3, but for 0030+3700.

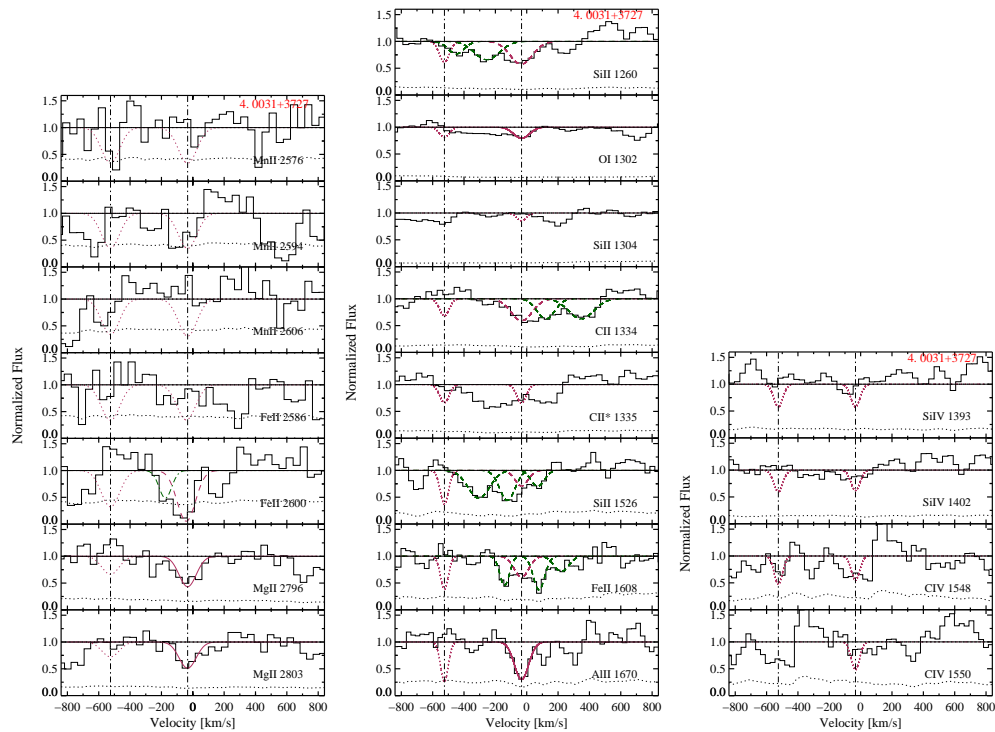


Figure 6. Same as Figure 3, but for 0031+3727.

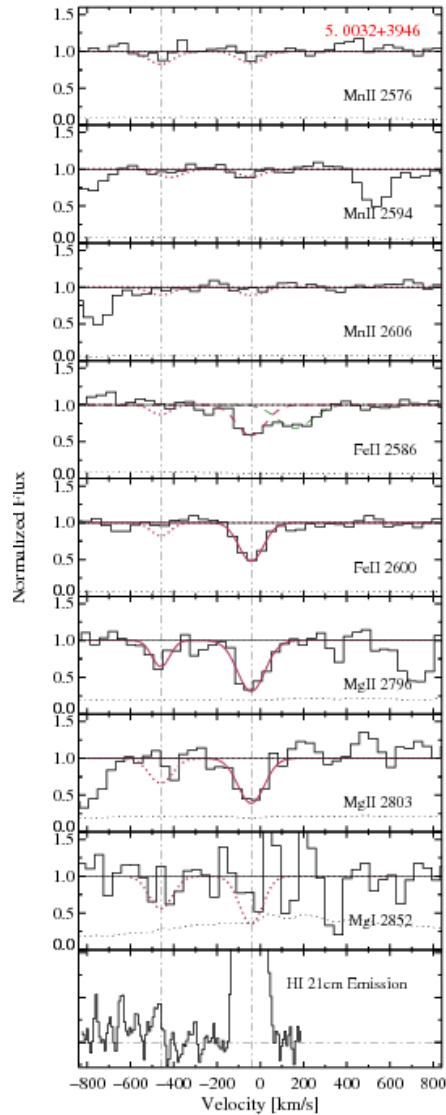


Figure 7. Same as Figure 3, but for 0032+3946. In addition, the HI 21 cm emission profile extracted from the GBT data of Thilker et al. (2004) is shown in the bottom panel. The intensities are scaled to accentuate the very weak emission signal from M31. The dash-dot horizontal line drawn in the 21 cm panel marks the location of zero intensity. No FUV spectra of this quasar were obtained.

the Si II $\lambda 1260$ and C IV $\lambda 1548$ lines had to be deblended from overlapping unrelated absorption. Given that the 21 cm emission extends over a large range in velocity, we cannot rule out that all the absorption features within the C IV $\lambda 1548$ blend are due to C IV $\lambda 1548$ absorption over a wide velocity range. Confirmation would require a

higher signal-to-noise spectrum; here, we identify the lowest velocity component with the M31 C IV $\lambda 1548$ absorption line. The low-ions are centered at ~ -336 km s $^{-1}$ and the high-ions are centered at ~ -340 km s $^{-1}$. However, Mg II and Fe II absorption lines from M31 gas were not detected. The GBT data show that 21 cm emission from M31 exists

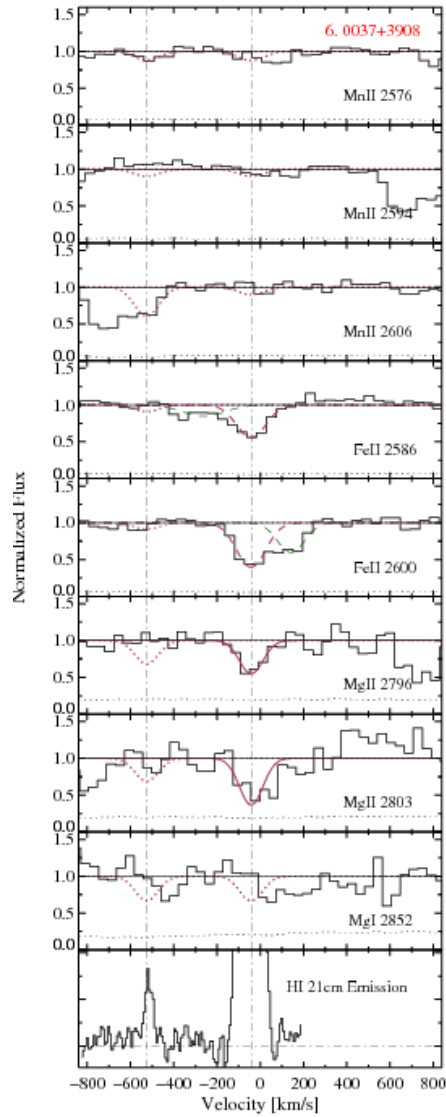


Figure 8. Same as Figure 7, but for 0037+3908. No FUV spectra were obtained for this quasar.

along this sightline between -559 km s^{-1} and -326 km s^{-1} , with a total integrated column density of $N_{\text{HI}} = 1.2 \times 10^{19}$ atoms cm^{-2} . We note that the absorption-line velocities are coincident with the peak in the 21 cm emission-line spectrum (bottom panels of Figure 10). Many significant Galactic absorption lines are present. Galactic Si II $\lambda 1260$ and C IV $\lambda 1550$ had to be deblended to separate them out from unrelated overlapping absorption.

9. 0043+4234 ($b = 17.4 \text{ kpc}$, $\lambda_{\text{forest}} < 1448 \text{ \AA}$, **Fig. 11**):

The sightline to this quasar passes “above” the H I 21 cm emission disk of M31 on the receding, northwest, side (see Figure 1). Due to the location of the sightline, the detected M31 and Galactic absorption lines needed to be deblended from each other. We used two-component Gaussian fits with fixed velocity components to do this. Measurements of the Si II $\lambda 1260$, C II $\lambda 1334.5$ (and C II* $\lambda 1335.7$), Si IV $\lambda 1393$,

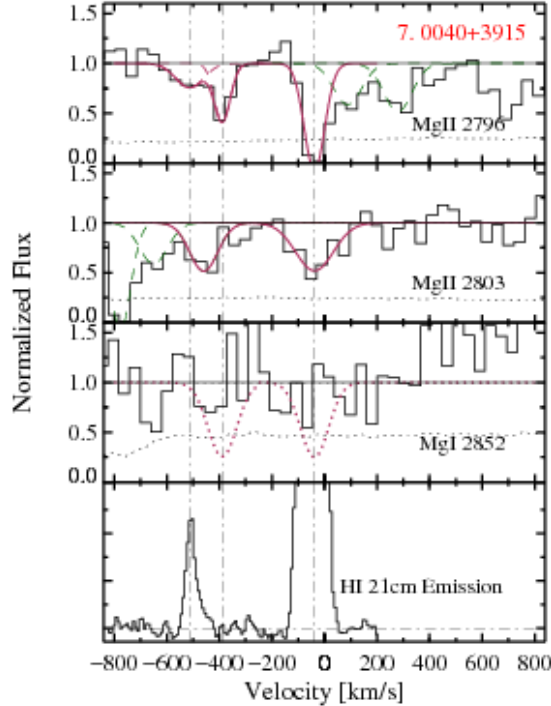


Figure 9. Same as Figure 7, but for 0040+3915. The M31 HVC that is detected in 21 cm at -513 km/s, is also detected in the Mg II $\lambda 2796$ line. The two Mg II $\lambda 2803$ components are too weak to be resolved with these data. The FUV data are not shown because the spectrum had no flux presumably due to an intervening Lyman limit system.

and Al II $\lambda 1670$ absorption lines are further complicated by other overlapping absorption. For low-ion absorption the velocity centroid for the Galactic lines was fixed using Mn II $\lambda 2576$, while allowing the position of the M31 low-ion velocity centroid to vary until the best least-squares solution was found. Deblending indicates that the detected M31 low-ion gas, which gives rise to transitions of Si II, C II, Al II, Fe II and Mg II, is located at -234 km s $^{-1}$, and the Galactic low-ion gas is located at -73 km s $^{-1}$. It is notable that along this sightline there is a detection of Galactic C II* $\lambda 1335.7$. The M31 high-ion gas, which gives rise to transitions of Si IV $\lambda 1393$ and C IV $\lambda 1548$, are also members of a multi-component blend with Galactic lines. Using a procedure similar to the one used for the low-ions, we find that the M31 high-ion gas is at -191 km s $^{-1}$ and the Galactic high-ion gas is at -1 km s $^{-1}$. GBT data reveal M31 21 cm emission between -259 km s $^{-1}$ and -93 km s $^{-1}$, with a total integrated column density of $N_{HI} = 8 \times 10^{18}$ cm $^{-2}$ (see §2.1). The higher velocity edge of the M31 21 cm emission is uncertain since it may overlap with Galactic 21 cm emission.

10. 0046+4220 ($b = 17.5$ kpc, $\lambda_{forest} < 1588$ Å, Fig. 12):

The sightline to this quasar passes through the H I 21 cm emission disk of M31 on the north side along its major

axis, as well as through two HVCs (see Figure 1). As with sightline 9, detected M31 and Galactic absorption lines needed to be deblended from each other. We followed the same general procedure followed for sightline 9. Measurements of the Si II $\lambda 1260$, O I $\lambda 1302$, Si II $\lambda 1304$, C II $\lambda 1334.5$ (and C II* $\lambda 1335.7$), Si II $\lambda 1526$, C IV $\lambda 1548$, and Al II $\lambda 1670$ absorption lines are further complicated by overlapping or nearby absorption. Deblending indicates that the detected M31 low-ion gas, which gives rise to transitions of Si II, O I, C II, Al II, Fe II and Mg II, is located at -195 km s $^{-1}$, and the Galactic low-ion gas is located at -40 km s $^{-1}$. As with sightline number 9, it is notable that along this sightline there is a detection of Galactic C II* $\lambda 1335.7$. Deblending results on M31 high-ion gas, which is apparent in C IV but possibly not Si IV, suggests the gas is located at -152 km s $^{-1}$, and the Galactic high-ion gas is located at -35 km s $^{-1}$. The GBT observations are shown in the bottom panels of the figure. An inset in one of the bottom panels shows the entire 21 cm profile; the primary emission peak is from M31 and the secondary peak near 0 km s $^{-1}$ is Galactic emission. The vertical dot-dashed lines in the inset are at the same velocities as in the panel. The 21 cm emission disk component of M31, which has an integrated column density of $N_{HI} = 1.5 \times 10^{21}$ cm $^{-2}$ (see §2.1), is detected

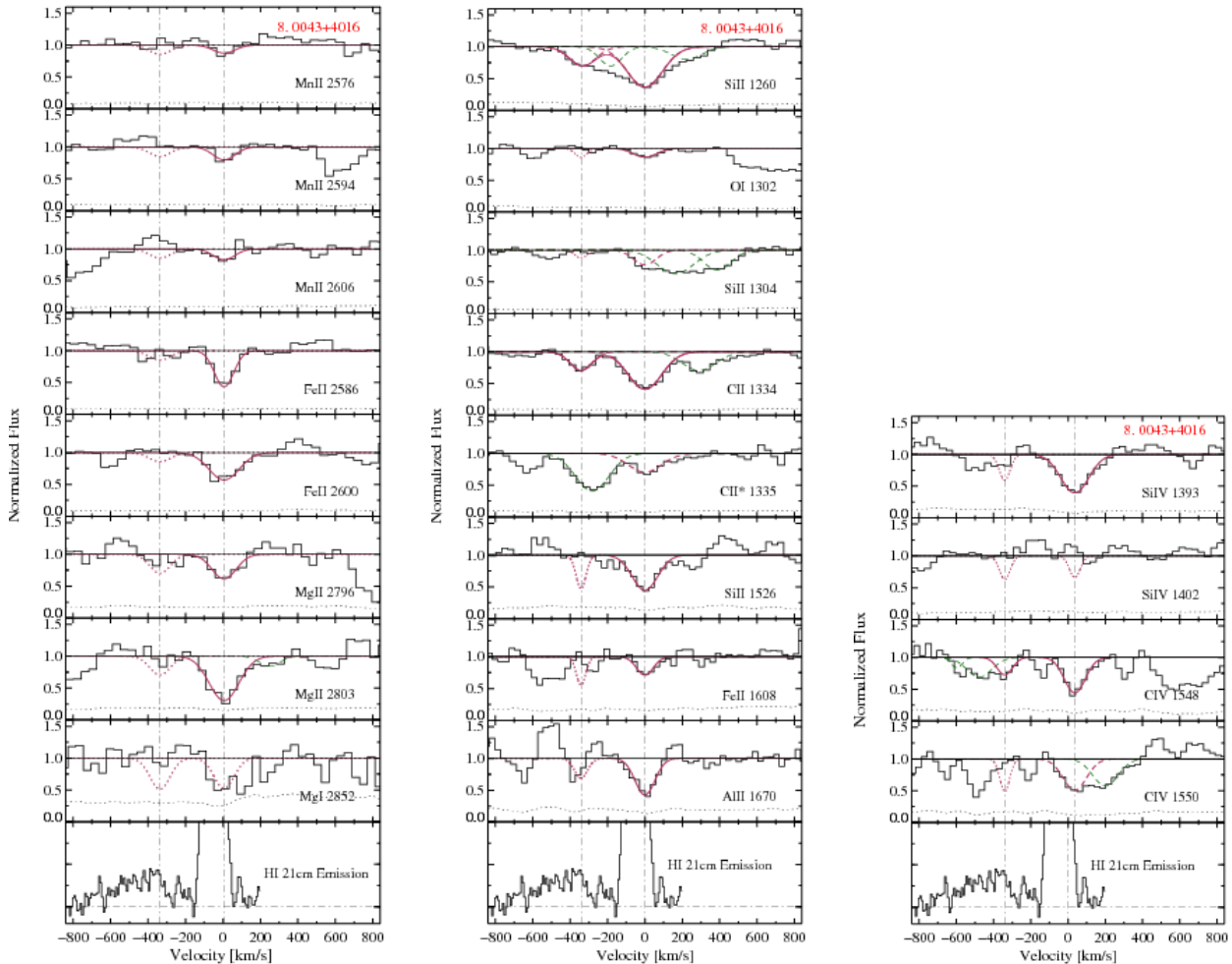


Figure 10. Same as Figure 7, but for 0043+4016. FUV data obtained for this quasar are also shown.

between -276 km s^{-1} and -27 km s^{-1} . These velocities fall in the range of the detected low-ion and high-ion M31 gas. We note that, based on evaluation of the 21 cm emission results, this is the only system which reaches DLA HI column densities (i.e., $N_{\text{HI}} \geq 2 \times 10^{20} \text{ atoms cm}^{-2}$). DLAs are the quasar absorption-line systems used to track the evolution of neutral gas in the Universe at low (Rao et al. 2006) and high (e.g., Noterdaeme et al. 2012) redshift. The strength of the M31 Mg II $\lambda 2796$ and Fe II $\lambda 2600$ absorption lines are consistent with criteria used in Mg II-selected DLA searches (Rao et al. 2006). The GBT observations also detect gas from two HVCs between -426 km s^{-1} and -392 km s^{-1} , and between -342 km s^{-1} and -326 km s^{-1} . The

total integrated column densities along the sightlines to the HVCs are $N_{\text{HI}} = 2.5 \times 10^{18} \text{ cm}^{-2}$ and $N_{\text{HI}} = 2 \times 10^{18} \text{ cm}^{-2}$ (see §2.1), respectively. We do not detect metal-line absorption near the velocities of these HVCs.

4 SUMMARY AND DISCUSSION OF RESULTS FOR M31

4.1 Overview on the Detection of Low-Ion and High-Ion Absorption Lines

The detections of M31 gas presented in the previous section and reported in Tables 3 and 4 can be summarized as follows.

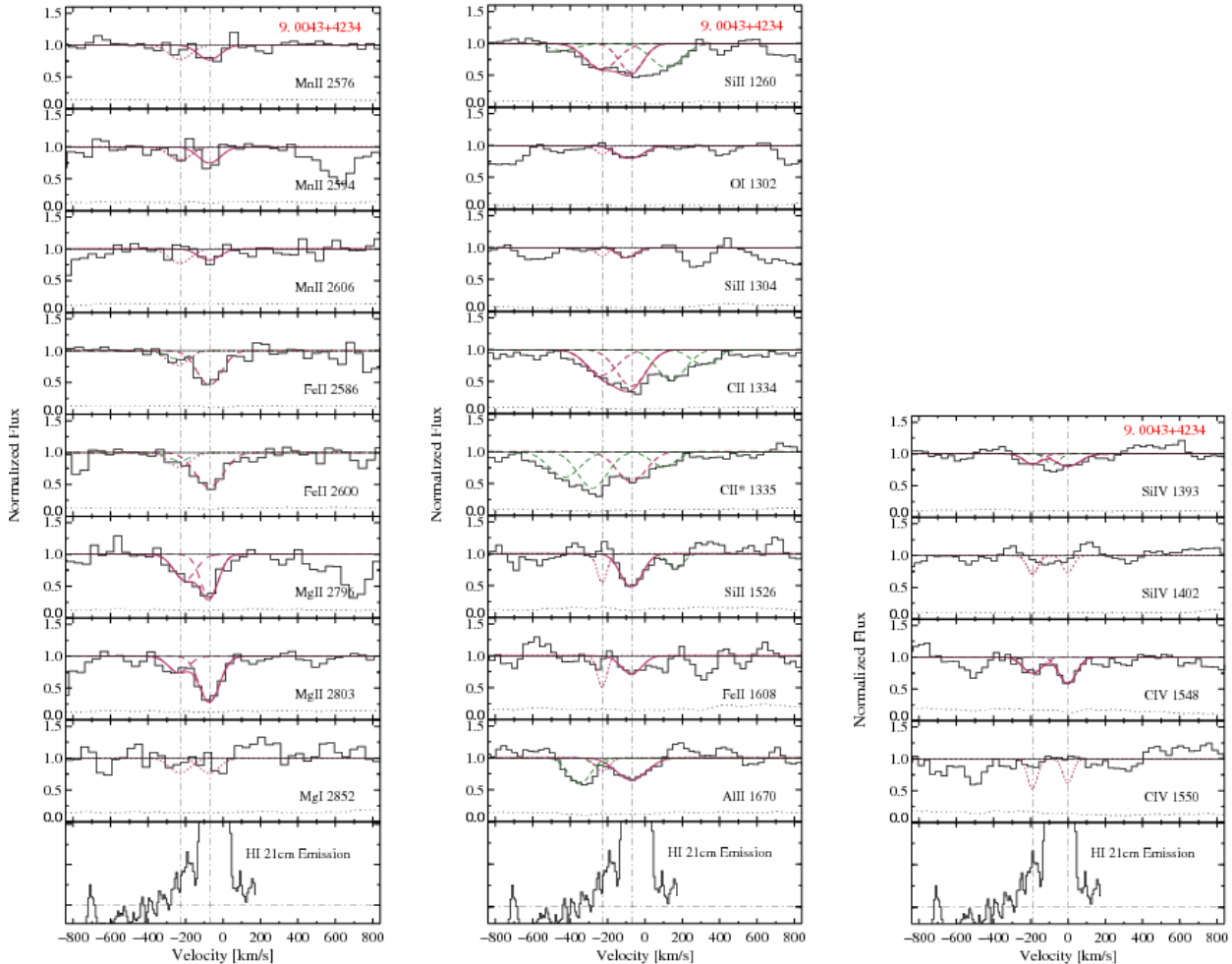


Figure 11. Same as Figure 7, but for 0043+4234. FUV data obtained for this quasar are also shown.

Low-ion Mg II absorption due to M31 gas is detected along four of the 10 observed sightlines (numbers 5, 7, 9, and 10). These sightlines have impact parameters ranging between $b \approx 17$ and 32 kpc. We also detect other low-ion gas (e.g., due to Si II, O I, C II, Fe II, or Al II) along three of the four sightlines with Mg II detections; the other sightline (number 5) was not observed in the FUV, where most of these transitions occur. In addition, we detect C II absorption at M31 velocities along sightline number 8 ($b = 13.4$ kpc). Sightline number 6 ($b = 30.5$ kpc) is the only “inner” sightline which does not show evidence for M31 low-ion absorption ($W_0^{\lambda 2796} < 0.41$ Å); however, no FUV spectra were obtained along this sightline. Among these “inner”

sightlines, the Mg II rest equivalent widths ranged between $W_0^{\lambda 2796} \approx 0.34$ and 0.71 Å, with the strongest detection being a two-component absorber with $W_0^{\lambda 2796} \approx 0.30$ and 0.41 Å. The four outer sightlines (numbers 1 through 4), with impact parameters $b \approx 57$ to 112 kpc, do not show Mg II absorption down to 2σ rest equivalent upper limits ranging between $W_0^{\lambda 2796} \approx 0.21$ and 0.46 Å.

High-ion C IV absorption due to M31 gas is detected along three of six sightlines (numbers 8, 9, and 10) which have usable FUV spectra. These three detections are all in “inner” sightlines, with impact parameters ranging between $b \approx 13$ and 18 kpc, and rest equivalent widths ranging between $W_0^{\lambda 1548} \approx 0.17$ and 0.65 Å. Some Si IV absorption and

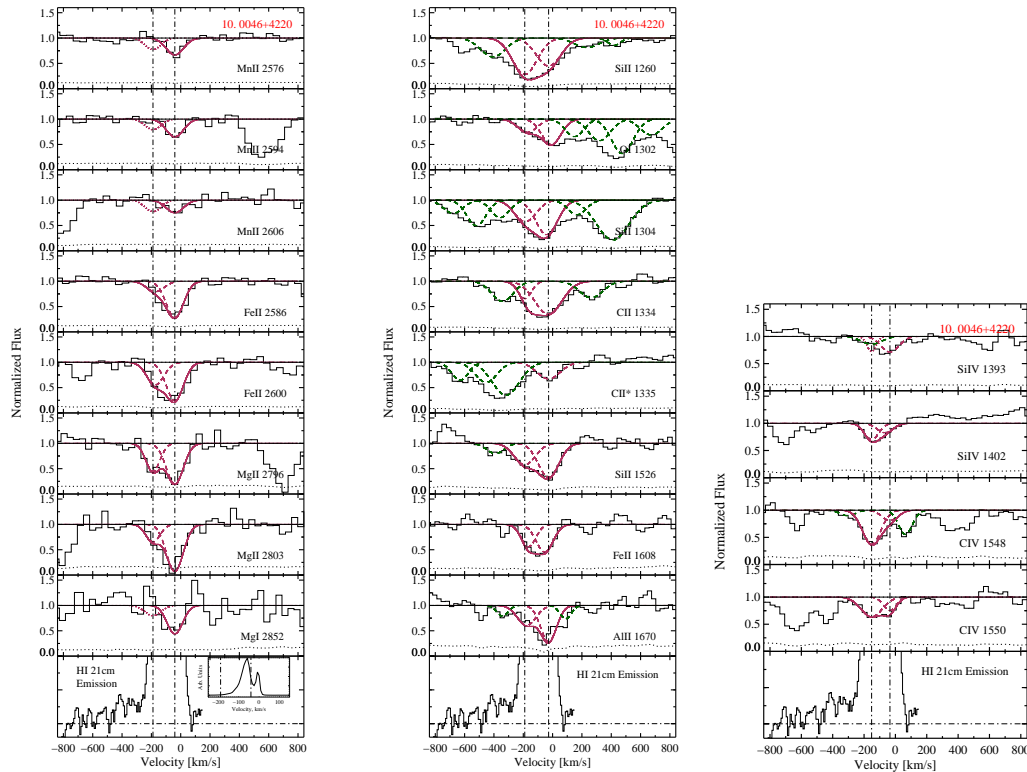


Figure 12. Same as Figure 7, but for 0046+4220. FUV data obtained for this quasar are also shown.

low-ion absorption is also detected along these three “inner” sightlines. The three C IV non-detections are in outer sightlines (numbers 1, 3, and 4), with impact parameters ranging between $b \approx 57$ and 112 kpc, and with 2σ rest equivalent width upper limits ranging between $W_0^{\lambda 1548} \approx 0.18$ and 0.30 Å.

We should point out that many of the detections summarized above were near the limit of our sensitivity threshold, despite the fact that our rest equivalent width upper limits are typical of those in large optical quasar absorption-line surveys. Another concern is confusion from overlapping or nearby absorption, but we believe we have dealt with this appropriately.

Also, Rich et al. (private communication) has observed three sightlines in the halo of M31 with COS. They do not cover the Mg II region, but detect C IV from M31 in some of these sightlines. There are other HST archival observations in the M31 halo, but these do not show any detections.

4.2 Implications

As elaborated further in §4.3, a clear picture does emerge. The absorption lines that arise in M31 gas are found to be relatively weak in comparison to those often identified in optical quasar absorption-line surveys, and even more so in comparison to absorption lines which arise in the ISM of the Milky Way Galaxy (e.g., Table 3). Moreover, none of the detected M31 absorption lines are found at large impact parameters. This could also be viewed as unexpected since the bulk of intervening low- to moderate-redshift metal-line absorbers seen in quasar spectra are identified with large-impact-parameter galaxies in followup imaging studies (e.g., Rao et al. 2011, Chen et al. 2010). However, all of the large-impact-parameter sightlines we observed were generally along M31’s major axis, so one scenario which might explain the lack of absorption in those cases would be to hypothesize that extended gaseous absorption originates in galactic fountains and preferentially avoids extended regions along the direction of the disk (e.g., Bordoloi et al. 2011, Bouché et al. 2012). Alternatively, M31 may simply be typical of a class of luminous galaxies that don’t possess large

Table 3. Rest Equivalent Width Measurements^a

Line	1.0018+3412 REW (Å)	2.0024+3439 REW (Å)	3.0030+3700 REW (Å)	4.0031+3727 REW (Å)	5.0032+3946 REW (Å)	6.0037+3908 REW (Å)	7.0040+3915 REW (Å)	8.0043+4016 REW (Å)	9.0043+4234 REW (Å)	10.0046+4220 REW (Å)
M31 Absorption Lines										
SiII1260	0.113	...	0.300	0.132	0.225 ± 0.042	0.259 ± 0.054	0.544 ± 0.042
OII1302	0.113	...	0.093	0.065	0.048	0.048	0.187 ± 0.047
SiII1304	0.043	0.046	0.341 ± 0.036
SiII1334	0.106	...	0.303	0.121	0.192 ± 0.042	0.318 ± 0.039	0.234 ± 0.044
CaII* 1335	0.131	...	0.373	0.118
SiIV1393	0.145	...	0.205	0.143	0.139	0.085 ± 0.042	< 0.095
SiIV1402	0.131	...	0.188	0.137	0.125	0.098	0.156 ± 0.065
SiII1526	0.173	...	0.523	0.214	0.180	0.152	0.386 ± 0.066
FeII1608	0.223	...	0.384	0.209	0.151	0.168	0.267 ± 0.076
AlII1670	0.244	...	0.453	0.253	0.194	0.110	0.258 ± 0.087
CIV1548	0.202	...	0.298	0.180	0.146 ± 0.061	0.167 ± 0.087	0.651 ± 0.098
CIV1550	0.175	0.161	0.320 ± 0.070
MnII2576	0.447	0.274	0.307	0.829	0.218	0.150	...	0.181	0.285	0.156 ± 0.065
MnII2594	0.422	0.283	0.302	0.815	0.139	0.123	...	0.187	0.263	0.243
MnII2606	0.428	0.291	0.311	0.829	0.138	0.498	...	0.182	0.285	0.257
FeII2586	0.421	0.254	0.435	0.847	0.178	0.120	...	0.187	0.289	0.266 ± 0.115
FeII2600	0.430	0.291	0.313	0.865	0.133	0.114	...	0.183	0.291	0.571 ± 0.112
MgII2796	0.459	0.261	0.211	0.433	0.341 ± 0.171	0.405	0.304 ± 0.220 ^b	0.379	0.554 ± 0.111	0.627 ± 0.112
...	0.412 ± 0.256 ^b
MgII2803	0.484	0.248	0.226	0.354	0.430	0.399	0.606 ± 0.208	0.377	0.285 ± 0.117	0.390 ± 0.122
MgII2852	0.619	0.387	0.419	...	0.565	0.428	0.981	0.624	0.301	0.260
Milky Way Absorption Lines										
SiII1260	0.289 ± 0.054	...	0.358 ± 0.081	0.320 ± 0.053	0.636 ± 0.048	0.689 ± 0.044	0.479 ± 0.056
OII1302	0.189 ± 0.086	...	0.071	0.113 ± 0.042	0.107 ± 0.021	0.162 ± 0.032	0.358 ± 0.050
SiII1304	0.258 ± 0.033	...	0.065	0.050	0.154 ± 0.029	0.084 ± 0.032	0.545 ± 0.045
CaII 1334	0.410 ± 0.095	...	0.448 ± 0.128	0.309 ± 0.048	0.594 ± 0.034	0.592 ± 0.036	0.669 ± 0.032
CaII* 1335	0.129	...	0.401	0.115	0.295 ± 0.044	0.413 ± 0.044	0.288 ± 0.039
SiIV1393	0.131	...	0.396 ± 0.121	0.144	0.533 ± 0.036	0.149 ± 0.056	0.189 ± 0.095
SiIV1402	0.108	...	0.163	0.130	0.116	0.104	0.133 ± 0.065
SiII1526	0.286 ± 0.046	...	0.462	0.155 ± 0.097	0.483 ± 0.062	0.706 ± 0.093	0.761 ± 0.092
FeII1608	0.231	...	0.372	0.243 ± 0.092	0.175 ± 0.076	0.119 ± 0.060	0.424 ± 0.078
AlII1670	0.634 ± 0.063	...	0.557	0.443 ± 0.102	0.427 ± 0.082	0.274 ± 0.066	0.440 ± 0.099
CIV1548	0.213 ± 0.077	...	0.471 ± 0.261	0.155	0.270 ± 0.110	0.252 ± 0.078	0.264 ± 0.079
CIV1550	0.365 ± 0.074	...	0.299	0.177	0.378 ± 0.095	0.128	0.132 ± 0.066
MnII2576	0.417	0.356 ± 0.106	0.722	0.849	0.205	0.150	...	0.135 ± 0.067	0.297 ± 0.112	0.427 ± 0.093
MnII2594	0.428	0.285	0.317	0.838	0.133	0.123	...	0.222 ± 0.074	0.325 ± 0.104	0.448 ± 0.100
MnII2606	0.438	0.273	0.310	0.884	0.143	0.136	...	0.190 ± 0.082	0.226 ± 0.113	0.319 ± 0.100
FeII2586	0.627 ± 0.222	0.626 ± 0.126	0.667 ± 0.163	0.838	0.602 ± 0.142	0.659 ± 0.078	...	0.632 ± 0.077	0.767 ± 0.147	0.919 ± 0.092
FeII2600	0.591 ± 0.162	0.676 ± 0.139	0.671 ± 0.172	1.209 ± 0.312	0.646 ± 0.062	0.897 ± 0.131	...	0.755 ± 0.104	0.888 ± 0.186	0.965 ± 0.094
MgII2796	0.869 ± 0.179	0.968 ± 0.146	1.058 ± 0.115	0.726 ± 0.133	1.025 ± 0.215	0.569 ± 0.199	0.977 ± 0.293	0.580 ± 0.194	0.764 ± 0.107	1.096 ± 0.122
MgII2803	0.508 ± 0.198	0.947 ± 0.135	0.846 ± 0.110	0.624 ± 0.117	0.870 ± 0.220	1.038 ± 0.248	0.089 ± 0.288	1.294 ± 0.211	0.920 ± 0.096	1.249 ± 0.120
MgII2852	0.626	0.493	0.595	...	0.833	0.428	0.959	0.608	0.304	0.846 ± 0.117

^a2 σ upper limits are tabulated for non-detections.

^bThe two measurements are M31 HVC and disk components, respectively. See Figure 9.

gaseous cross sections which are capable of giving rise to moderate-strength quasar absorption lines. Our findings for M31 may in some way be connected to the observed relative decrease in the incidence of stronger Mg II systems with decreasing redshift (e.g., Nestor et al. 2005).

In the past several years there has been speculation that M31 is a galaxy that lies in the “green valley (e.g., Mutch et al. 2011, Davidge et al. 2012). The idea is that it exhibits properties that put it between the red cloud and blue cloud populations that have been identified in large galaxy surveys. Such galaxies may be in a stage of transition and their star formation may nearly cease in less than 5 Gyrs. While this may be the case for M31, we note that the data we have discussed here should not be taken to offer any clues about this. For example, our data do not allow us to draw any conclusions about the strength of star formation or even the column densities of metal-line absorption. This is because the lines we have identified are likely to be mostly saturated. Thus, the weakness of the metal-line absorption in M31 most likely indicates that the effective gas velocity spread is low; it may either be truly low relative to the spectral resolution and/or there may be a small number of velocity components within the spectral resolution element.

4.3 Mg II Rest Equivalent Width ($W_0^{\lambda 2796}$) versus Impact Parameter (b)

Figure 13 is a plot of M31 Mg II $\lambda 2796$ rest equivalent width ($W_0^{\lambda 2796}$) detections (or 2σ upper limits) versus sightline impact parameter (b). The measurement shown for quasar number 7, which has $b = 26.9$ kpc, was made by fitting a single Gaussian to both absorption components reported in Table 3, i.e., it is not a simple sum of the results from the two individual Gaussian fits reported in Table 3. Since the impact parameters of quasar numbers 9 and 10 are very similar, they are displaced from each other in the figure for clarity. Note that the upper limits are 2σ upper limits, while the error bars are the 1σ uncertainties. The four outermost data points are suggestive of an overall decrease of $W_0^{\lambda 2796}$ with increasing impact parameter. Quasar absorption line studies of large samples of absorber-galaxy pairs have shown this to be true as well (Chen et al. 2010; Rao et al. 2011).

For comparison, Figure 14 includes results from the Rao et al. (2011) sample of absorbing galaxies which have been identified for Mg II-selected DLAs, subDLAs, and Lyman limit systems (LLSs). The mean redshift of the Rao et al. sample is $z \sim 0.5$, with redshifts in the range $0.1 \lesssim z \lesssim 1.0$. The identified absorbing galaxies in the Rao et al. sample also have a range luminosities, mostly $0.1 \lesssim L \lesssim 1.0L^*$, but there is not a significant correlation between luminosity and

impact parameter. Rao et al. found only a marginal (1.8σ) correlation between $W_0^{\lambda 2796}$ and b . The solid black circles in Figure 14 are DLAs and the open circles are subDLAs and LLSs. The data from this current M31 study are in red, and the encircled data point (sightline 10) is the only one where the integrated 21 cm emission H I column density, averaged over a spatial scale of ~ 50 pc, is in the DLA regime. Sightlines 5 through 9 have averaged integrated 21 cm emission H I column densities in the subDLA regime. H I 21 cm emission maps are not available as far out as the four outermost sightlines, but since the $N_{HI} = 1.9 \times 10^{18} \text{ cm}^{-2}$ edge of the H I disk of M31 is at $b \approx 33$ kpc (Figure 1), these sightlines are not expected to have averaged integrated H I column densities in the DLA or subDLA regime.

Thus, as noted in §4.1 and §4.2, it is clear that the sightlines passing near M31, or through its gaseous disk seen in 21 cm emission, do not give rise to the moderate-to-strong Mg II absorption lines which are often identified in moderate- to high-redshift quasar absorption-line surveys. For example, although the number of M31 sightlines is still only ten, none of the 6 sightlines through the H I 21 cm emission disk have $W_0^{\lambda 2796} > 0.7 \text{ \AA}$. For comparison, all of the Galactic detections reported in Table 3 have $W_0^{\lambda 2796} > 0.5 \text{ \AA}$, and 5 of the Galactic sightlines have $W_0^{\lambda 2796} \sim 1 \text{ \AA}$. In the HST Key Project sample of Galactic sightlines (Savage et al. 2000) the median value is $W_0^{\lambda 2796} = 1.17 \text{ \AA}$, and the strongest line has $W_0^{\lambda 2796} = 2.2 \text{ \AA}$.

Of course, our sightlines through M31 are biased sightlines in the context of traditional absorption line surveys, in that the galaxy was pre-selected in order to study the properties of its low-ion and high ion-gas. Therefore, for M31 the probability of occurrence of Mg II absorption as a function of $W_0^{\lambda 2796}$ is not properly estimated from the observed incidence of Mg II absorption in unbiased quasar absorption-line surveys. Instead, however, this experiment does show that a gas-rich, $\sim 2L^*$, spiral galaxy like M31 need not give rise to moderate-to-strong Mg II absorption along sightlines which pass through its H I 21 cm emission disk, or even through a putative extended gaseous halo.

4.4 Comparison of 21 cm Emission and Absorption-Line Velocities

The range of velocities that exhibit 21 cm emission for sightline numbers 5 through 10 are shown as cyan and orange vertical bars as a function of impact parameter in Figure 15. Cyan bars correspond to 21 cm emission velocities from the disk and orange bars represent HVC velocities. Also plotted are the velocities of the low-ion (red stars) and high-ion (blue triangles) absorption lines from Table 4. For the two inner disk sightlines (numbers 9 and 10 at ≈ 17.5 kpc), it appears that the velocity of the high-ion absorption is better correlated with the 21 cm emission velocity range. Along sightline number 8, the low and high-ion absorption lie at an outer velocity edge of where 21 cm emission is detected. As noted in §3, this velocity corresponds to the peak in 21 cm emission along this sightline. For sightline numbers 7 (at $b = 26.9$ kpc) and 5 (at $b = 31.5$ kpc), the low-ion gas again coincides with the peak of 21 cm emission which is near the edge of the 21 cm profile (see Figures 7 and 9). Thus, in nearly all cases, the low ions occur near the edge of the 21 cm profiles (two are near the low velocity edge and three

are near the high velocity edge), and for sightlines 5, 7, and 8, are coincident with the peak in 21 cm emission.

Given the resolution of the NUV and FUV data ($\sim 87 \text{ km s}^{-1}$ at $\sim 2800 \text{ \AA}$ and $\sim 106 \text{ km s}^{-1}$ at $\sim 1550 \text{ \AA}$), one might question if these differences are significant. However, it is well-known that in data with sufficient signal-to-noise, a Gaussian fit to an absorption line can be used to determine the centroid location of the line to an accuracy much better than the line’s FWHM. In order to determine how accurately absorption-line locations can be determined, we ran 10,000 realizations of lines with equivalent widths drawn from the data. Figure 16 shows the distributions of equivalent widths. Noise was added to the Gaussian profiles generated with these equivalent widths so that the resulting signal-to-noise ratios matched the data. Line centroids were then estimated by refitting Gaussian profiles to the noised-up absorption lines. The resulting distributions of centroid velocities relative to the input values are shown in Figure 17. For both the original as well as the simulated data, the spectra were rebinned to two pixels per resolution element before measurements were made. The signal-to-noise ratios of NUV spectra were, in general, higher than in FUV spectra. Thus, the accuracy with which the line centroids can be measured is higher for the Mg II lines. Specifically, the centroid standard deviation of the Mg II distribution is $\sim 6 \text{ km s}^{-1}$ compared to $\sim 16 \text{ km s}^{-1}$ for C IV. These uncertainties indicate that the separations in velocities of the low and high ions are significant towards sightline numbers 9 and 10 at approximately the 2σ level.

The 21 cm emission studies of M31 (e.g., §2.1) show that for this nearly edge-on galaxy, the sightline velocities of gas giving rise to 21 cm emission can span a large range (e.g., see the lower panels in Figures 3 – 12). Corbelli et al. (2010) fitted a tilted ring model to M31’s H I 21 cm emission data from 8 to 37 kpc to study the details of its rotation, finding that M31’s disk warps beyond galactocentric distances of ~ 25 kpc and that it becomes more inclined with respect to our sightline. As we have shown above, the Mg II absorption regions are almost always at the peak of the 21 cm emission profile, which occurs near the edge of the 21 cm emission velocity range. Thus, when detected, the low-ion gas appears to trace the 21 cm gas. Interestingly, neither low- nor high-ion absorption lines are detected at the 21 cm velocity locations of the HVCs towards quasar number 10 ($b = 17.5$ kpc). Low-ion absorption is also not detected at the 21 cm disk velocity location towards quasar number 6 ($b = 30.5$ kpc). In fact, the observed low-ion absorption along sightline number 7 originates in the HVC detected in 21 cm emission, however at the velocity location of the other absorption component, there is no detected 21 cm emission. This component, at -389 km s^{-1} , is likely to be M31 halo gas. Thus, it appears that the sightlines through M31 are passing through very different physical and kinematic conditions within its ISM.

5 CONCLUSIONS

A conventional study relating quasar absorption-lines to the galaxies that cause them begins with the detection of an intervening absorption-line system in a spectrum followed by imaging work to identify the galaxy. The experiment with

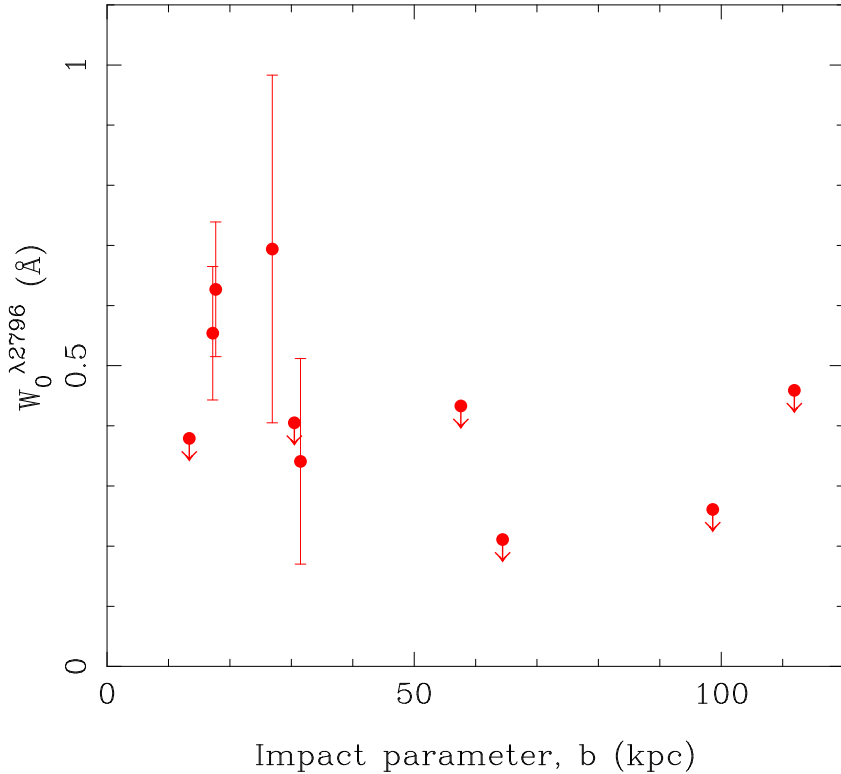


Figure 13. Mg II $\lambda 2796$ rest equivalent width, $W_0^{\lambda 2796}$, vs. impact parameter, b , for M31 measurements from Table 3. Detections have 1σ error bars and arrows indicate 2σ upper limits for the non-detections. For quasar 7, which is the data point at 26.9 kpc, a single Gaussian fit solution to the HVC and M31 components is shown. It has $W_0^{\lambda 2796} = 0.694 \pm 0.289$ Å. The two points at $b \sim 17.5$ kpc have been displaced for clarity.

Table 4. Heliocentric velocity offsets of low- and high-ion absorption lines^a

Quasar	M31		Milky Way	
	Low ion (km s ⁻¹)	High ion (km s ⁻¹)	Low ion (km s ⁻¹)	High ion (km s ⁻¹)
1. 0018+3412	-18	-61
2. 0024+3439	-6	...
3. 0030+3700	-21	-53
4. 0031+3727	-33	...
5. 0032+3946	-453	...	-42	...
6. 0037+3908	-508	...	-42	...
7. 0040+3915	-513, -389 ^b	...	-38	...
8. 0043+4016	-336	-340	6	42
9. 0043+4234	-234	-191	-73	-1
10. 0046+4220	-195	-152	-40	-35

^aThe velocity centroid of the Milky Way absorption system is determined from the Mn II $\lambda 2576$ line, if detected, or from the Mg II $\lambda 2796$ line if no Mn II is present, or from the C II $\lambda 1334$ if neither is present in the spectrum. The velocity centroid of the C IV $\lambda 1548$ line was determined independent of the low-ion velocity, and was used to constrain the positions of the high-ionization lines. The uncertainties in the low- and high-ion velocities are 6 km s⁻¹ and 16 km s⁻¹, respectively.

^bThe two measurements are M31 HVC and halo components, respectively. See Figure 9.

M31 described here is a quasar absorption-line survey conducted in reverse. We probed ten sightlines with vastly different impact parameters through a single spiral galaxy with a luminosity of $\sim 2L^*$. As summarized in §4.1, we detected some type of absorption from M31 gas in five of the six inner sightlines ($13 < b < 32$ kpc), but no absorption in any of the

four outer sightlines ($57 < b < 112$ kpc). We also reported the first detection of metals in a M31 HVC.

In §4.3 we compared our M31 results to the findings in the conventional Rao et al. (2011) survey. Rao et al. found only a marginal anticorrelation between $W_0^{\lambda 2796}$ and b , and indeed we find the same qualitative trend in M31, but the

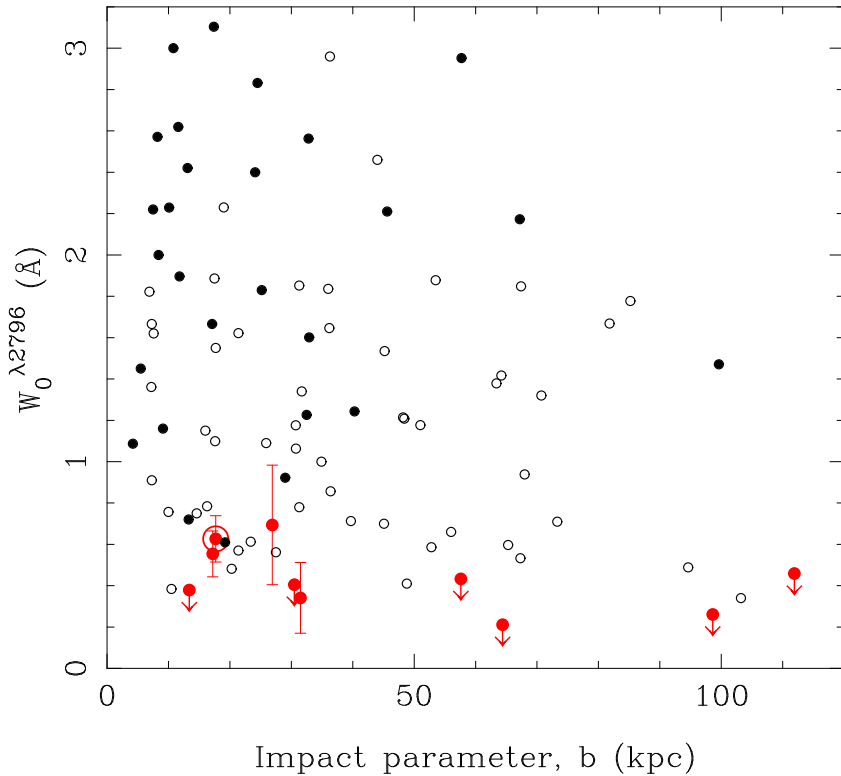


Figure 14. Same as Figure 13, but data points from Rao et al. (2011) have been added. These represent identified galaxy impact parameters for Mg II systems with H I column density measurements at $z \sim 0.5$. Solid black circles are the DLAs as measured in UV spectra (Rao, Turnshek, & Nestor 2006) and open black circles are subDLAs and LLSs. The DLA system in M31 (inferred from its integrated column density using 21 cm emission observations with GBT), sightline 10, is the red encircled point.

values of $W_0^{\lambda 2796}$ are far smaller in M31 (Figure 14). And while Rao et al. found that there were fewer systems with moderate-to-strong $W_0^{\lambda 2796}$ at large- b ($b > 50$ kpc), we found none arising in M31. In §4.4 we compared the velocity locations of low-ion and high-ion gas in M31 to that of M31’s 21 cm emission and found that the high-ion gas is better aligned with the velocities of observed 21 cm emission along two of three sightlines where it is detected. The velocity of the low-ion gas is correlated with the peak of 21 cm emission and is often near the edge of the 21 cm emission velocity range. In one case Mg II is detected at a velocity location that shows no 21 cm emission.

Broadly, our results indicate that:

(i) Despite the fact that M31 is a gas-rich, $\sim 2L^*$ spiral galaxy, it produces relatively weak Mg II and C IV absorption lines in comparison to those found in moderate-to-high redshift quasar absorption-line surveys. For Mg II, this may indicate that M31 is typical of a class of luminous galaxies that don’t possess gaseous cross sections capable of giving rise to moderate-strength quasar absorption lines even at impact parameters $b \lesssim 32$ kpc. This finding might also be related to the observed relative decrease in the incidence of stronger Mg II systems with decreasing redshift.

(ii) M31 appears not to possess an extensive large gaseous cross section at impact parameters $b > 57$ kpc that is capable of giving rise to moderate-strength quasar absorption lines (e.g., with $W_0^{\lambda 1548} > 0.2$ Å or $W_0^{\lambda 2796} > 0.3$ Å), at least not along the direction of its major axis.

(iii) For the relatively weak absorption that we did detect at $b \lesssim 32$ kpc, we found the low-ion gas to be associated with the peak in the 21 cm emission profile, near one edge of the 21 cm emission velocity range. Two of three sightlines showed high-ion gas to be centrally located within the 21 cm emission profile, with the third being coincident with an edge. It is also likely that we have detected low-ion halo gas through one of the sightlines.

Future UV spectroscopy of quasars behind M31 can build on these findings by: (1) acquiring higher signal-to-noise data to probe down to weaker rest equivalent width values, (2) acquiring higher resolution data to better study the velocity locations of the gas relative to 21 cm emission velocities, and/or (3) probing a larger number of sightlines including ones in M31’s extended halo region.

It would be interesting if N_{HI} results derived from M31’s 21 cm emission data could be compared with N_{HI} determinations from Lyman series absorption seen in the UV spectra of background quasars. One could then get an H I column density measurement averaged over less than a milli-parsec region in M31, in comparison to the ~ 50 pc linear spatial scale offered by the radio observations. This would provide information on the homogeneity and size scale of H I absorbing regions in M31.

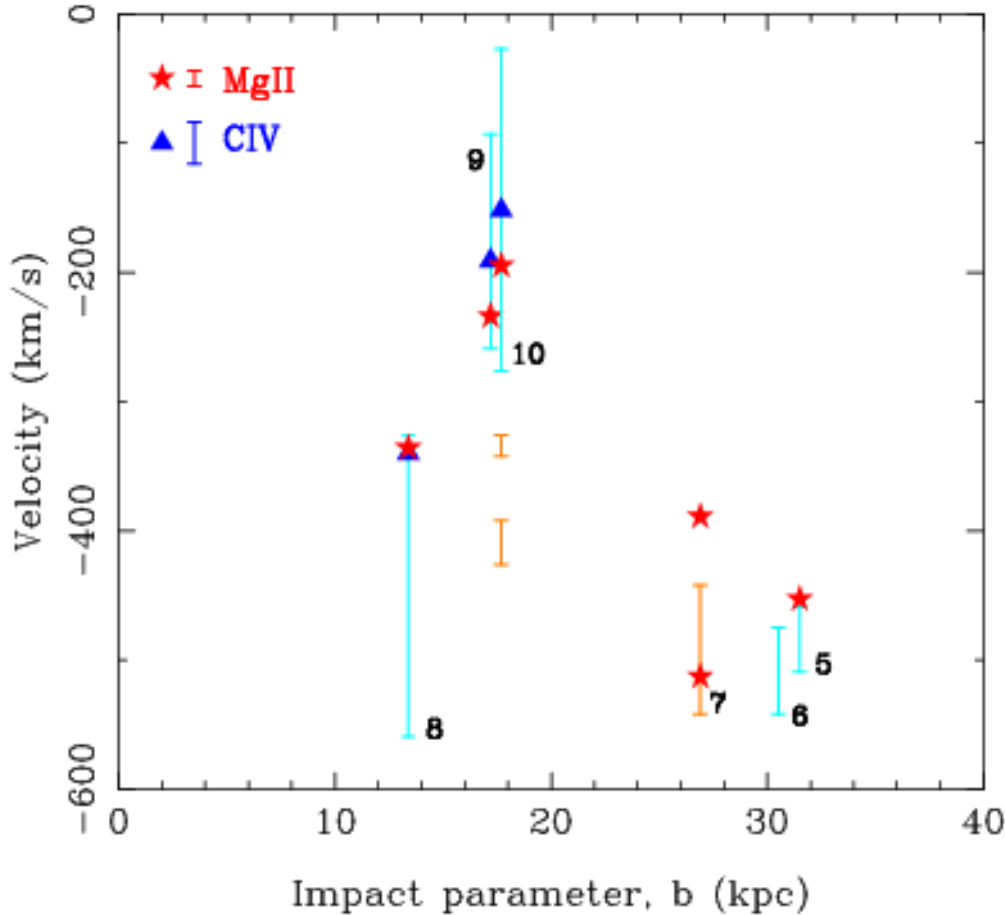


Figure 15. Velocities of detected lines in M31 as a function of impact parameter. Cyan and orange vertical bars represent velocity ranges of 21 cm emission from M31’s disk and HVCs, respectively. (See the bottom panels of Figures 7-12.) Red stars are low-ion (Mn II, Mg II, or C II) line centroids, and blue triangles are high-ion (C IV) line centroids from Table 3. The uncertainty in the velocity measurement is shown as the vertical bar in the upper left corner. Sightlines 9 and 10 are displaced for clarity. Three distinct velocity ranges are apparent towards sightline 10; the wide component arises in the disk of M31 and the two narrower components originate in M31 HVCs. The two red stars along sightline 7 are the two components of the Mg II line shown in Figure 9. 21 cm emission is detected only from the HVC along this sightline but not at the velocity of the Mg II component at -389 km s^{-1} . We therefore surmise that this gas resides in the halo and not in the disk of M31. We caution that the velocities plotted in this figure are not a measurement of M31’s rotation curve since, except for sightline 10, the inner sightlines, i.e., 5-9, do not lie along the major axis of M31. See Figure 1.

ACKNOWLEDGMENTS

We are grateful for the referee’s encouraging remarks and comments which improved and clarified the paper. SMR, DAT, RW, DT, and DVB acknowledge support from HST grant GO-11658. GMS acknowledges support from a Zacheus Daniel Fellowship and a Dietrich School of Arts and Sciences Graduate Fellowship from the University of Pittsburgh. We are grateful for the help and support provided by the NOAO staff. We thank Michéle Belfort-Mihalyi for assisting on the NOAO observing run.

REFERENCES

- Abraham, S., Philip, N. S., Kembhavi, A., Wadadekar, Y. G., & Sinha, R. 2012, MNRAS, 419, 80
- Adelman-McCarthy, J. K., et al. 2006, ApJS, 162, 38
- Bergeron, J., & Boisse, P. 1991, A&A, 243, 344
- Bordoloi, R. et al. 2011, ApJ, 743, 10
- Bouché, N., Hohensee, W., Vargas, R., Kacprzak, G. G., Martin, C. L., Cooke, J., & Churchill, C. W. 2012, MNRAS, 426, 801
- Braun, R., Thilker, D. A., Walterbos, R. A. M., & Corbelli E. 2009, ApJ, 695, 937
- Chen, H.-W., Helsby, J. E., Gauthier, J.-R., Schectman, S. A., Thompson, I. B., & Tinker, J. L. 2010, ApJ, 714, 1521
- Cool, R. J., et al. 2012, ApJ, 748, 10
- Corbelli, E., Lorenzoni, S., Walterbos, R., Braun, R., & Thilker, D. 2010, A&A, 511, 89
- Davidge, T., et al. 2012, ApJ, 751, 74
- de Vaucouleurs, G., de Vaucouleurs, A., Corwin, H. G., Jr., Buta, R. J., Paturel, G., & Fouqué, P. 1991, Third Reference Catalogue of Bright Galaxies (New York: Springer)
- Evans, I. N., et al. 2010, ApJS, 189, 37
- Fardal, M. A., Babul, A., Geehan, J. J., & Guhathakurta, R. 2006, MNRAS, 366, 1012

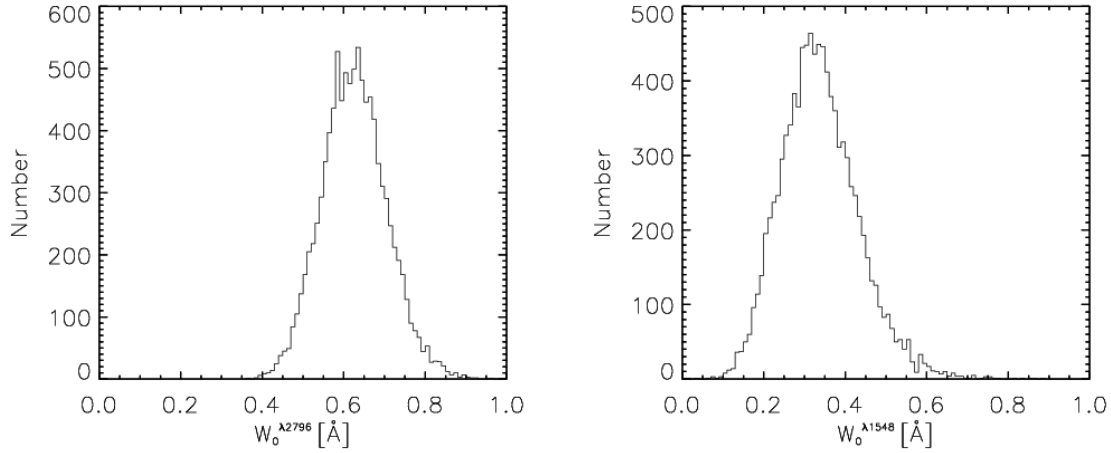


Figure 16. Distribution of rest equivalent widths, Mg II $W_0^{\lambda 2796}$ (left) and C IV $W_0^{\lambda 1548}$ (right), from 10,000 realizations of the data.

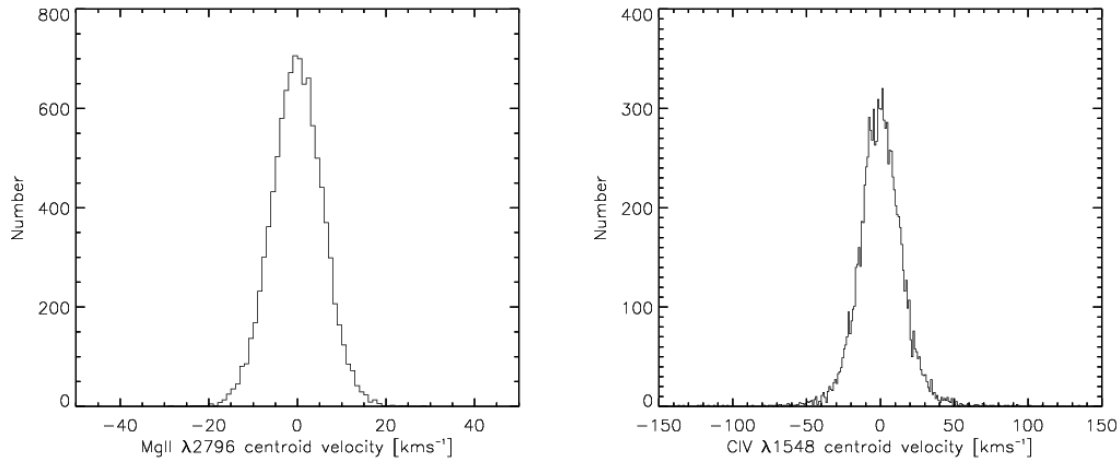


Figure 17. Distribution of line centroid velocity offsets measured from 10,000 realizations of the data. Gaussian profiles with rest equivalent widths sampled from measured values were generated, to which noise was added to match the signal-to-noise ratio of the data. Centroid velocities of these simulated lines were measured, and the offsets from input values are shown here. We report the standard deviation of this distribution as the uncertainty in the centroid velocity measurement, i.e., the Mg II $\lambda 2796$ and C IV $\lambda 1548$ line centroids can be measured with an accuracy of 6 km s^{-1} and 16 km s^{-1} , respectively.

Lanzetta, K., Turnshek, D., & Wolfe, A. 1987, *ApJ*, 322, 739
 Lanzetta, K., & Bowen, D. 1990, *ApJ*, 357, 321
 Mutch, S. J., Croton, D. J., & Poole, G. B. 2011, *ApJ*, 736, 84
 Nestor, D., Turnshek, D., & Rao, S. 2005, *ApJ*, 628, 637
 Nestor, D., Turnshek, D., & Rao, S. 2006, *ApJ*, 643, 75
 Richards, G. T., Myers, A. D., Gray, A. G., Riegel, R. N., Nichol, R. C., Brunner, R. J., Szalay, A. S., Schneider, D. P., & Anderson, S. F. 2009, *ApJS*, 180, 67
 Rao, S., Turnshek, D., & Nestor, D. 2006, *ApJ*, 636, 610
 Rao, S. M., Belfort-Mihalyi, M., Turnshek, D. A., Monier, E. M., Nestor, D. B., & Quider, A. M. 2011, *MNRAS*, 416, 1215
 Riess, A., Fliri, J., & Valls-Gabaud, D. 2012, *ApJ*, 745, 156
 Savage, B. D. et al. 2000, *ApJS*, 129, 563
 Steidel, C. 1993, *The Environment and Evolution of Galaxies*, Astrophysics and Space Sciences Library Vol 188 (Kluwer), eds. M. Shull and H. Thronson, p263
 Tamm, A., Tempel, E., Tenjes, P., Tihhonova, O., & Tuvikene, T. 2012, *A&A*, 546, 4
 Thilker, D., Braun, R., Walterbos, R., Corbelli, E., Lockman, F.,

Murphy, E., & Maddalena, R. 2004, *ApJ*, 601, L39
 Tollerud, E. J., Beaton, R. L., Geha, M. C., et al. 2012, *ApJ*, 752, 45
 Westmeier, T., Braun, R., & Thilker, D. 2005, *A&A*, 436, 101
 Weymann, R. J., et al. 1998, *ApJ*, 506, 1